physchem

MDPI

Article

Vibrational Analysis of Benziodoxoles and Benziodazolotetrazoles

Seth Yannacone, Kapil Dev Sayala, Marek Freindorf, Nicolay V. Tsarevsky and Elfi Kraka *

Department of Chemistry, Southern Methodist University, 3215 Daniel Avenue, Dallas, TX 75275, USA; syannacone@smu.edu (S.Y.); ksayala@smu.edu (K.D.S.); mfreindorf@smu.edu (M.F.); nvt@smu.edu (N.V.T.)
* Correspondence: ekraka@smu.edu; Tel.: +1-214-768-2611

Abstract: Tetrazoles are well known for their high positive enthalpy of formation which makes them attractive as propellants, explosives, and energetic materials. As a step towards a deeper understanding of the stability of benziodazolotetrazole (BIAT)-based materials compared to their benziodoxole (BIO) counterparts, we investigated in this work electronic structure features and bonding properties of two monovalent iodine precursors: 2-iodobenzoic acid and 5-(2-iodophenyl)tetrazole and eight hypervalent iodine (III) compounds: *I*-hydroxybenzidoxolone, *I*-methoxybenziodoxolone, *I*-ethoxybenziodoxolone, *I*-*iso*-propoxybenziodoxolone and the corresponding *I*-hydroxyben ziodazolotetrazole, *I*-methoxybenziodazolotetrazole, *I*-ethoxybenziodazolotetrazole and *I*-*iso*-propoxybenziodazolotetrazole. As an efficient tool for the interpretation of the experimental IR spectra and for the quantitative assessment of the I−C, I−N, and I−O bond strengths in these compounds reflecting substituent effects, we used the local vibrational mode analysis, originally introduced by Konkoli and Cremer, complemented by electron density and natural bond orbital analyses. Based on the hypothesis that stronger bonds correlate with increased stability, we predict that, for both series, i.e., substituted benziodoxoles and benziodazolotetrazoles, the stability increases as follows: *I*-*iso*-propoxy < *I*-ethoxy < *I*-methoxy < *I*-hydroxy. In particular, the I−N bonds in the benziodazolotetrazoles could be identified as the so-called trigger bonds being responsible for the initiation of explosive decomposition in benziodazolotetrazoles. The new insight gained by this work will allow for the design of new benziodazolotetrazole materials with controlled performance or stability based on the modulation of the iodine bonds with its three ligands. The local mode analysis can serve as an effective tool to monitor the bond strengths, in particular to identify potential trigger bonds. We hope that this article will foster future collaboration between the experimental and computational community being engaged in vibrational spectroscopy.

Keywords: hypervalent iodine; vibrational spectroscopy; local vibrational mode theory; density functional theory; benziodazolotetrazoles; benziodoxoles; high-energy materials; explosives

Citation: Yannacone, S.; Sayala, K.D.; Freindorf, M.; Tsarevsky, N.V.; Kraka, E. Vibrational Analysis of Benziodoxoles and Benziodazolotetrazoles. *Physchem* **2021**, *1*, 45–68. https://doi.org/10.3390/physchem1010004

Academic Editors: Sergei Manzhos and Jacinto Sá

Received: 27 March 2021
Accepted: 5 May 2021
Published: 14 May 2021

1. Introduction

Organic polyvalent iodine (III) and (V) reagents have gained popularity as oxidants, electrophiles, and radical sources in various synthetically useful organic transformations [1–8], as well as in organometallics [9], materials, and polymer chemistries [10]. These compounds contain an iodine atom which bonds to a carbon atom via conventional 2-center-2-electron (2c-2e) covalent bond, but also to two or more ligands (L) via 3-center-4-electron (3c-4e) bonds [11,12], dubbed *hypervalent* (HV) [13]. According to this model, only p-orbitals of the central atom are involved in the formation of the 3c-4e bonds. Since publication of the aforementioned pioneering works, a number of additional studies have appeared in the literature discussing in more detail the nature of HV bonds [14–17]. The presence of weak HV bonds is largely responsible for the characteristic structural features of HV iodine (HVI) molecules (e.g., presence of the near-linear L−I−L fragment(s)), as well as for their stability and reactivity [18,19]. Donor atoms of the ligands must be electronegative (e.g., F, O, N, or Cl) to promote stability. Among said ligands, carboxylates are the most widely studied and HVI(III) compounds such as (dicarboxyloxy)iodo

arenes ($ArI(O_2CR)_2$) [20] with linear arrangements of O atoms from the ligands and the central iodine atom) and benziodoxoles (where the carboxylate ligand and the HVI atom form a ring) [8,21] have found numerous applications. Tetrazolates (RCN_4^-) resemble carboxylates (RCO_2^-) in many respects (e.g., basicity, nucleophilicity, and complexation ability [22]), which prompted Tsarevsky et al. to investigate the propensity of tetrazole (TZ) for bonding to iodine(III) atoms. Several examples of TZ-containing HVI(III) compounds were synthesized and studied, including acyclic [23], pseudocyclic (with iodonium-like structure) [24], and heterocyclic benziodoazotetrazole (BIAT) derivatives [25]. Each of these compounds, like their carboxylate analogues, are strong oxidants. However, unlike the caboxylates, when heated BIATs decompose vigorously and even explosively. TZs are well known for their high positive enthalpy of formation (ΔH_f) [26–29], which makes them attractive as propellants, explosives, and energetic materials [30], but HV compounds with one or more tetrazolate ligands are markedly more unstable than the parent free ligands [23,24].

An important question has been raised: which molecular parameters make TZs so explosive, and, even more importantly, how can their thermal stability be controlled. To answer this question, Tsarevsky et al. determined the enthalpies of thermal decomposition (ΔH_d) for BIAT derivatives with axial Cl, OH, OMe, and OAc ligands. However, they did not find any significant correlation between ΔH_d and structural parameters (e.g., lengths of either of the HV bonds or L−I−N valence angles), nucleophilicity, or field electronic parameters of the ligand [25]. It has been suggested that crystal packing in the solid state, i.e., the shearing force between packing layers may well account for the (in)stability of TZs, influencing both temperatures of decomposition and ΔH_d, which complicates any direct comparison between ΔH_d and structural parameters [31–33]. A common way to answer this question from a theoretical perspective is to use bond dissociation energies (BDE) [34,35] as a tool to identify the so-called *trigger bond*, which is first to break and therefore assesses the stability of a material [36]. However, a caveat is needed. BDE is not a suitable way to measure the intrinsic strength of a chemical bond because it also contains geometry relaxation and electronic structure reorganization of the dissociated fragments [37–43]. Therefore, this work refers to the local vibrational mode (LMV) theory originally proposed by Konkoli and Cremer [44–48], which provides a quantitative measure of intrinsic bond strength based on vibrational spectroscopy [49].

As a step towards understanding more about the nature and stability of TZ-based energetic materials from an electronic structure perspective, this work investigates the iodine-containing bond strengths in two precursor monovalent iodine compounds, 2-Iodobenzoic acid (**IBA**) and 5-(2-Iodophenyl)tetrazole (**IPT**), as well as in HVI(III) compounds derived thereof, namely substituted BIOs **1–4** and BIATs **5–8** (shown in Figure 1), utilizing local vibrational force constants derived from LVM. This work is complemented with electron density information and natural bond orbitals (NBOs) to assess and predict chemical bond properties which correlate with explosive capabilities, and to explore the suggestion that a strongly positive molecular center (i.e., iodine) may serve as a reliable indicator for sensitive materials [50–52]. In addition, this work applies another feature of the LMV theory: the comprehensive analysis of experimental (*exp*) IR spectra [46,48]. An overarching aim of this research is to inspire the experimental and theoretical chemistry communities working in the field of vibrational spectroscopy to foster future collaborations.

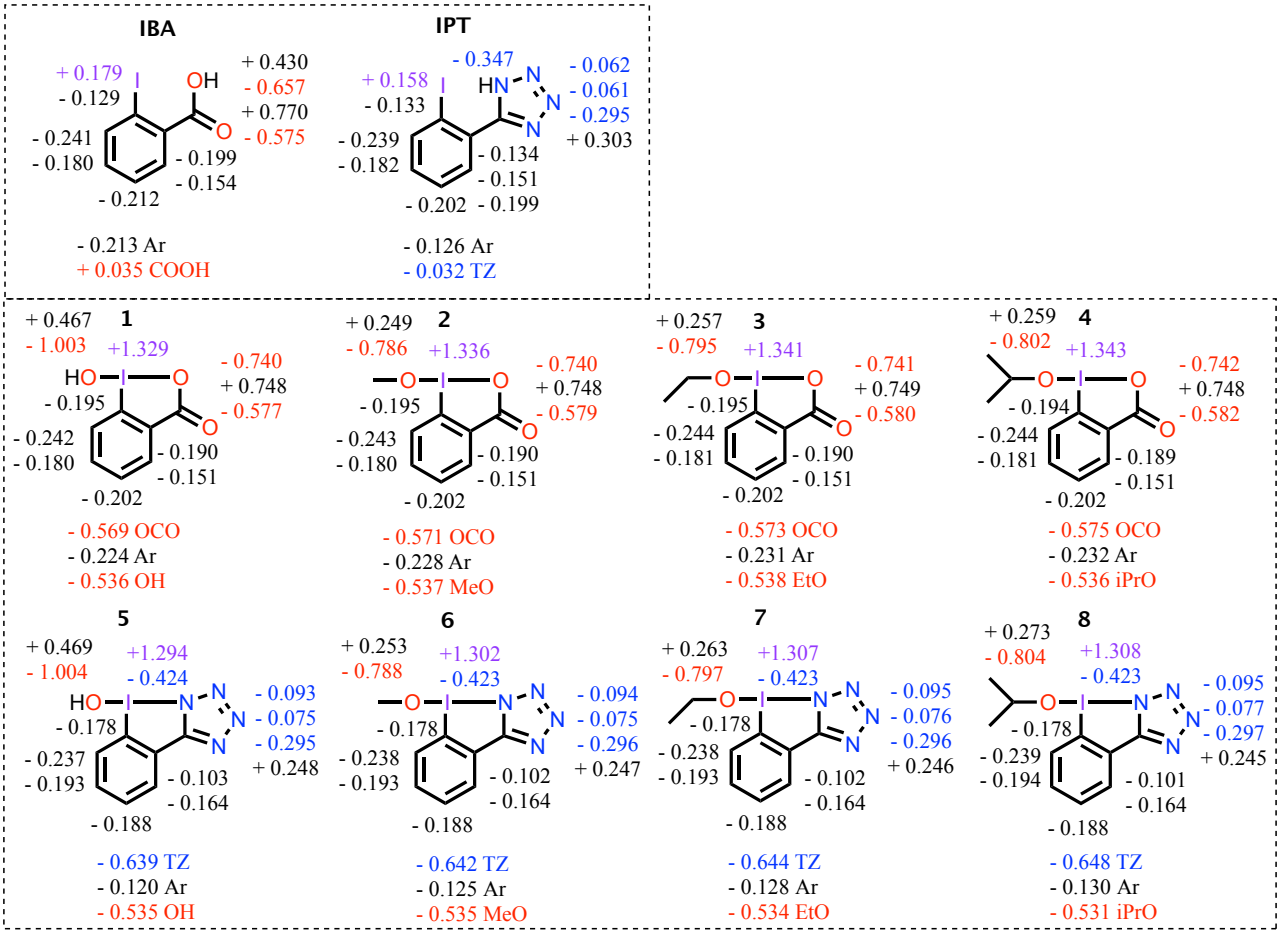

Figure 1. Schematic of reference molecules **IBA** and **IPT**, BIOs **1–4** and BIATs **5–8**, showing atomic NBO charges (units in [*e*]) of iodine (purple), oxygen (red), carbon/hydrogen (black), and nitrogen (blue); calculated at the ωB97X-D/Def2-TZVP level of theory. Summed NBO charges of hydroxyl/alkoxy, carboxylate ester (OCO), tetrazole (TZ), and *ortho*-substituted benzene (Ar) groups are shown below each respective molecule. Note: For BIOs **2–4** and BIATs **6–8**, the charges shown in black font to the left of molecule numbers are the total charges of the Me, Et, and iPr groups, respectively.

2. Computational and Experimental Methods

To validate the model chemistry used in this work, experimental geometry coordinates and IR frequencies of BIO-**1** (see Tables 1 and 2) were utilized as benchmarks for several levels of theory. Table 1 shows comparison between experimental (*exp*) and *theor* geometry parameters, and Table 2 summarizes the statistical analysis of *exp* IR frequencies ($\omega_{(exp)}$) and *theor* normal mode frequencies (ω_{μ}) of BIO-**1**; calculated using 13 levels of theory. The B3LYP [53–56], B3LYP-D3 [57], B3LYP-D3BJ [58], M06-2X [59], and ωB97X-D [60] density functionals were combined with the following basis sets: aug-cc-pVTZ-[PP for iodine] (acpVTZ-PP) [61–66], Def2-TZVP (TZVP) [67,68], Def2-TZVPP (TZVPP) [69,70]. The Def2-TZVPD basis set was also included, but only in combination with M06-2X because this level of theory was recently applied successfully for a computational study of phenomenal molecular systems containing λ^3-iodanes acting as biaxial halogen bond (XB) donors [71]. For the *theor* vibrational frequencies, the following scaling factors were applied to correct for the harmonic approximation of the Morse potential [72–79]: 0.968 (B3LYP/acpVTZ-PP), 0.965 (B3LYP/TZVP), 0.963 (B3LYP/TZVPP), 0.956 (M06-2X/acpVTZ-PP), 0.946 (M06-2X/TZVP), 0.957 (ωB97X-D/acpVTZ-PP), and 0.955 (ωB97X-D/TZVP) [73–79].

Table 1. Comparison of experimental and theoretical values of the bond length R (Å), the bond angle θ (Deg), and the dihedral angle φ (Deg) for BIO-**1**.

Parameter	exp [a]	ωB97X-D		B3LYP		M06-2X	
		acpVTZ	TZVP	acpVTZ	TZVP	acpVTZ	TZVP
R (I−C)	2.098	2.100	2.091	2.125	2.116	2.095	2.087
R (I−OR)	1.975	2.023	2.009	2.054	2.040	2.016	2.004
R (I−OCO)	2.274	2.131	2.121	2.160	2.150	2.124	2.113
θ (O−I−O)	167.5	169.7	169.8	169.9	170.0	169.1	169.3
θ (C−I−OR)	90.9	91.1	91.1	91.5	91.5	90.5	90.4
θ (C−I−OCO)	76.8	78.6	78.8	78.3	78.5	78.7	78.9
φ (O−C−O−I)	179.6	179.0	178.8	179.1	179.0	178.8	178.7
φ (C−C−O−I)	−1.9	−1.2	−1.4	−1.0	−1.2	−1.3	−1.5

[a] X-ray structure determined in this work. Details are provided in the Supplementary Materials.

Table 2. Comparison of experimental (*exp*) IR frequencies ($\omega_{(exp)}$) with theoretical (*theor*) normal mode vibrational frequencies (ω_μ) for BIO-**1**.

Model Chemistry	% Error (Average)	MAE	Standard Deviation	RMSE
ωB97X-D/acpVTZ-PP	1.81	16.44	21.13	26.35
ωB97X-D/TZVP	1.50	12.99	16.25	20.48
B3LYP/acpVTZ-PP	1.89	17.31	18.38	24.91
B3LYP/TZVP	2.11	19.06	17.67	25.69
B3LYP/TZVPP	2.12	18.82	19.02	26.41
B3LYP-D3/acpVTZ-PP	1.86	16.95	18.09	24.46
B3LYP-D3/TZVP	2.07	18.54	17.57	25.24
B3LYP-D3/TZVPP	2.05	18.00	19.10	25.89
B3LYP-D3BJ/acpVTZ-PP	1.77	16.38	17.73	23.81
B3LYP-D3BJ/TZVP	1.80	16.95	16.37	23.28
B3LYP-D3BJ/TZVPP	1.97	17.76	18.26	25.15
M06-2X/acpVTZ-PP	1.45	13.61	16.13	20.80
M06-2X/TZVP	2.17	22.04	17.25	27.72

Averages are based on 20 of the 21 *exp* IR frequencies (see below). MAE are given in cm^{-1}.

The results of the first attempts to determine the molecular structure of *I*-hydroxyben ziodoxolone (BIO-**1**) were published in 1964 by Shefter and Wolf [80], who noted that the endocyclic I−O bond was markedly longer (2.30 Å) than the sum of the covalent radii of the two atoms, which was attributed to steric strain or greater ionic character compared to the normal covalent I−O bond. A more detailed analysis, including all bond lengths and valence angles in the molecule, was provided a year later by the same authors [81]. Unfortunately, the published structure is imprecise (which becomes apparent by simple inspection of the clearly nonplanar benzene ring) and no further structural data have been reported since the publication of the two aforementioned papers. We therefore prepared crystals of BIO-**1** (by recrystallization from water) and were able to obtain a more accurate structure (Figure 2). The complete experimental details and structural data are provided in the Supporting Materials. This new structure was used for the analyses and comparison with the computed structural parameters, which allowed for proper selection of the computational method to be employed.

Calculations performed at the ωB97X-D/Def2-TZVP level of theory were in closest agreement with *exp* IR frequencies (average % error = 1.50, MAE = 12.99, standard deviation = 16.25, RMSE = 20.48), whereas comparison of *exp* and *theor* geometry parameters is less conclusive. Therefore, said model chemistry was utilized for the remainder of this work. All DFT calculations were performed with tight convergence criteria and superfine integration grids [82], and all stationary points were confirmed to be minima by the absence of imaginary normal mode frequencies.

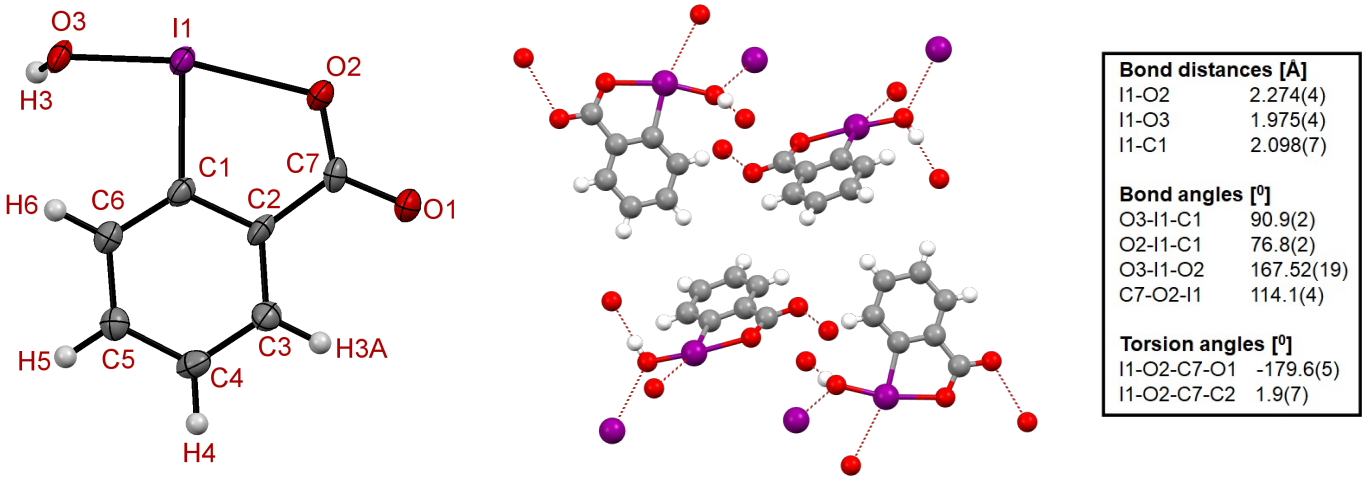

Figure 2. Displacement ellipsoid plot (50% probability level) of *I*-hydroxybenziodoxolone (BIO-**1**) at 100.0(3) K (left) and intermolecular secondary bonding in the crystals of BIO-**1** (center). Selected bond lengths, bond angles, and torsion angles are provided in the right hand-side panel.

In addition to serving as a popular analytical tool, modern vibrational spectroscopy [83–85] is an excellent source of information on the electronic structure a molecule. Specifically, a new quantitative measure for the intrinsic strength of a chemical bond is derived from vibrational force constants. However, one has to consider that normal vibrational modes are generally delocalized over the molecule due to coupling of the atomic motions [86–88]. Therefore, one cannot directly derive an intrinsic measure of bond strength from said normal modes, a fact that has already been discussed since the early days of vibrational spectroscopy. (The reader may refer to review articles, e.g., by Quack [89], Halonen [90], and Jensen [91] for a more in-depth discussion and to Ref. [49] for a historical overview.) Furthermore, it can be difficult to assign a peak on an experimental spectrum to a normal mode involving the vibrations of a particular functional group, particularly in the mid and lower frequency domains. Both problems are addressed by Local Vibrational Mode (LVM) theory, originally introduced by Konkoli and Cremer [44–48]. In Ref. [49], a comprehensive discussion of the underlying theory of LVMs is provided; therefore, in the following, only some essential features are summarized.

As outlined in Ref. [49], LVMs have a number of unique properties. Zou, Kraka, and Cremer [46,47] verified the uniqueness of the LVMs via an adiabatic connection scheme between local and normal vibrational modes. In contrast to normal mode force constants, LVM force constants have the advantage of not being dependent on the choice of coordinates used to describe the target molecule. The latter are highly sensitive to electronic structure differences (e.g., caused by changing a substituent) and directly reflect the intrinsic strength of a bond or weak chemical interaction, as has been shown by Zou and Cremer [92]. Thus, LVM stretching force constants have been utilized as a unique measure of the intrinsic strength of chemical bonds [38,39,48,93–104] and weak chemical interactions [19,40,105–126] based on vibrational spectroscopy. LVM theory has previously been applied for the description of bonding in a diverse set of 34 HVI compounds, the majority of which are λ^3-iodanes [19]. In this work, LVM theory and associated LVM stretching force constants were applied to investigate the I−C, I−N, and I−O bonds composing the 'T'-shaped molecular frameworks in a set of four BIATs and four BIOs.

In addition to local force constants and frequencies, the LVM analysis has led to a new way of analyzing vibrational spectra. Any normal vibrational mode $\mathbf{l}_\mu$ can be decomposed into LVM contributions [46,48], leading to detailed analysis of vibrational spectra and a wealth of information about structure and bonding [97,107]. Decomposition of normal modes into percent LVM contributions, also called *Characterization of Normal Modes* (CNM),

calculates for each normal mode $\mathbf{l}_\mu$ the overlap $S_{n\mu}$ with each local mode vector $\mathbf{a}_n^x$, with both vectors given in Cartesian coordinates $\mathbf{x}$, according to [46,48]:

$$S_{n\mu} = \frac{(\mathbf{a}_n^x, \mathbf{l}_\mu)^2}{(\mathbf{a}_n^x, \mathbf{a}_n^x)(\mathbf{l}_\mu, \mathbf{l}_\mu)}; \; with \; \mathbf{a}_n^x = \mathbf{L}\mathbf{a}_n \tag{1}$$

$(\mathbf{a}, \mathbf{b})$ in Equation (1) is the short notation for the scalar product of two vectors of $\mathbf{a}$ and $\mathbf{b}$

$$(\mathbf{a}, \mathbf{b}) = \sum_{i,j} a_i O_{ij} b_j \tag{2}$$

O_{ij} is an element of the metric matrix $\mathbf{O}$. We generally use the force constant matrix $\mathbf{f}^x$ as metric, namely $\mathbf{O} = \mathbf{f}^x$ to account for the influence of the electronic structure [46,48]. This leads to the contribution $C_{n\mu}$ of local mode $\mathbf{a}_n$ to the normal mode $\mathbf{l}_\mu$ given by:

$$C_{n\mu} = \frac{S_{n\mu}}{\sum_m^{N_{vib}} S_{m\mu}} \tag{3}$$

i.e., a completely localized normal mode $\mathbf{l}_\mu$ has a $C_{n\mu}$ value of 1 (corresponding to 100% if $C_{n\mu}$ is given as a percentage). The CNM procedure was recently applied to assess the usefulness of *Vibrational Stark Effect* probes [102], and to analyze π-hole interactions between aryl (Ar) donors and small molecule acceptors [126]. In this work, CNM is used to interpret *exp* and *theor* spectra.

DFT calculations were carried out with GAUSSIAN16 [127] and the standard frequency calculations were followed by LVM analysis, performed with the LModeA program [49,128]. The spectroscopic analysis was complemented with NBO populations calculated with the NBO6 package [129–131]. Electron densities ($\rho(\mathbf{r}_b)$) and energy densities ($H(\mathbf{r}_b)$) at the I−C, I−O, and I−N bond critical points $\mathbf{r}_b$ determined with the AIMAll package [132]. The covalent nature of the bonds was assessed following the Cremer–Kraka criterion, which implies that covalent bonding is characterized by a negative energy density, whereas electrostatic interactions are indicated by positive energy density values [133–135].

Commercially available **IBA** (98% purity) was purchased from Sigma-Aldrich, St Louis. **IPT**, BIO-**1** [25,136], and BIAT-**5** [25] were prepared using previously reported procedures. The identity and purity of synthesized compounds were confirmed by nuclear magnetic resonance (NMR) spectroscopy. Infrared (IR) spectra were collected on a Nicolet iS5 IR spectrometer with iD7 attenuated total reflectance (ATR) accessory and diamond crystal, and were formatted using OriginPro 9.1.0 (64 bit) [137]. Data were recorded in the domain of 4000–400 cm^{-1}. The number of scans were set to 16 with spectral resolution of 4 cm^{-1}. To ensure no contamination during the analysis, a background spectrum was collected every time before collecting the sample spectrum. All experiments were performed under ambient conditions.

3. Results/Discussion

3.1. Experimental and Theoretical IR-Spectra

Figure 3a,b show the *exp* and *theor* IR spectra of **IBA**, respectively. All *exp* compounds were in the solid phase under standard conditions, whereas *theor* normal mode vibrational frequencies were calculated in the gas phase. This difference in phase is responsible for the sharper, more well-defined peaks of the *theor* IR spectra. Additionally, corresponding peaks of the *theor* spectra have higher frequencies compared to the *exp* spectra which is also attributable to the phase difference. Discrepancies in peak height and shape are due to the signal intensities being given in transmittance for the *exp* spectra, and molar absorption coefficient (ε) for the *theor* spectra. To report the *exp* spectra with values of ε, amounts (i.e., film thickness or concentration) must be known and they are difficult to measure accurately using conventional spectral acquisition techniques. Likewise, to convert the *theor* spectra

to absorbance, concentrations must be known, which are irrelevant for isolated molecules in the gas phase.

The small peak at 3814 cm^{-1} of the *exp* spectrum corresponds with the peak at 3642 cm^{-1} of the *theor* spectrum. In this case, mapping the *exp* signal to the *theor* signal is straightforward because the *theor* peak at 3642 cm^{-1} is the highest normal vibrational mode, and the only signal close to 3814 cm^{-1}, with the nearest *theor* signal at 3086 cm^{-1}. Mapping *exp* to *theor* frequencies of lower resolution is less straightforward, but can be done by comparing IR intensities, using common functional group frequency characteristics, and comparing distances between signals. In the 3058 to 2510 cm^{-1} domain of the *exp* spectrum, there are six weak signals. The *theor* spectrum shows only one peak at 3086 cm^{-1}, but there are three more weak signals from 3093 through 3062 cm^{-1}, which have low intensities at the given scale. These *theor* peaks correspond with the *exp* peaks in the domain of 3058 through 2809 cm^{-1}. In both spectra, there are 14 prominent signals between 1800 and 400 cm^{-1}.

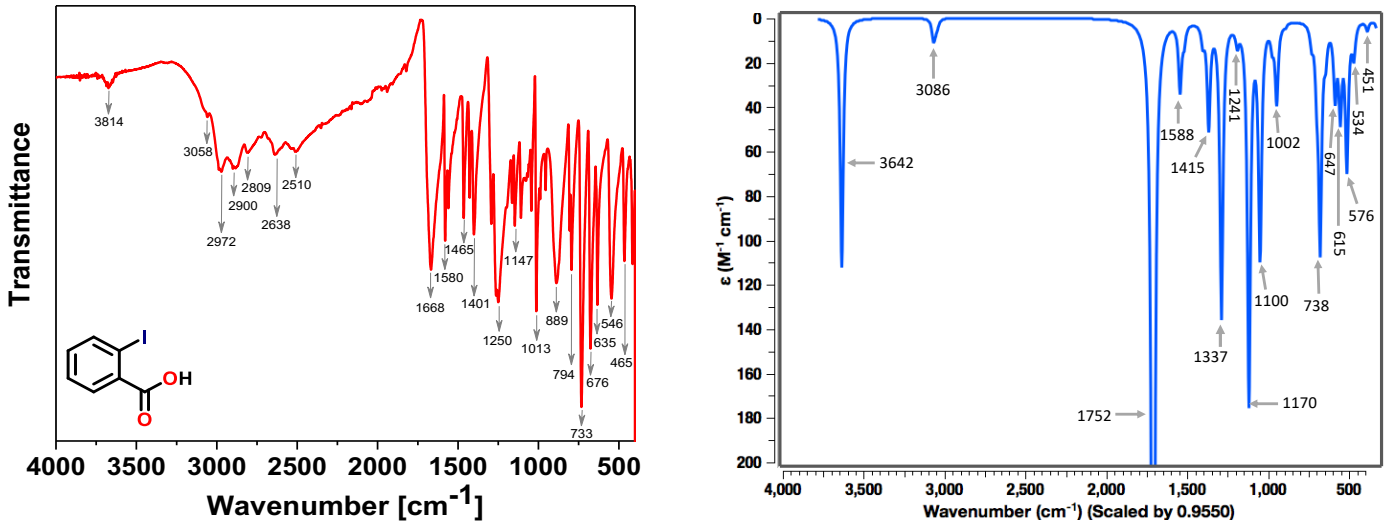

(**a**) (**b**)

Figure 3. (**a**) Experimental, and (**b**) theoretical IR spectra of **IBA**.

Figure 4a,b show the *exp* and *theor* IR spectra for **IPT**. There is an intense, sharp signal at 3507 cm^{-1} of the *theor* spectrum, which is not pronounced in the *exp* spectrum. This is likely due to the effects of intermolecular hydrogen bonding (HB) in the solid phase. Between 2900 and 2300 cm^{-1} of the *exp* spectrum, there is a multitude of signals, whereas there is only a single peak at 3084 cm^{-1} in the *theor* spectrum. As in the case of **IBA** for **IBA**, there are several low-intensity *theor* signals in the 3200 to 2800 cm^{-1} domain. On the other hand, none of the *exp* signals between 2700 and 2300 cm^{-1} are pronounced in the *theor* spectrum; this is also the case for the broad signal at 1823 cm^{-1}. From 1700 through 400 cm^{-1}, the signals match up well between *exp* and *theor* spectra.

Figure 5a,b are the *exp* and *theor* IR spectra of BIO-**1**, respectively. BIO-**1** is a *I*-hydroxylated HV derivative of the monovalent **IBA**. The *exp* and *theor* spectra of **IBA** are quite similar to the spectra of BIO-**1**. However, the spectra of **IBA** and BIO-**1** diverge in the 3100 to 2400 cm^{-1} domain, where BIO-**1** has fewer signals and no pronounced signals in the 3600 to 4000 cm^{-1} domain. In addition, the prominent signals at 733 and 1250 cm^{-1} of **IBA** have higher relative frequencies for BIO-**1**. Notably, the latter signal is nearly 90 cm^{-1} higher in BIO-**1**. For the *theor* spectrum of BIO-**1**, the peaks at 3701 and 3083 cm^{-1} have higher frequencies by 59 and 3 cm^{-1}, respectively, compared to the corresponding signals of **IBA**. On the other hand, many of the signals between 1800 and 400 cm^{-1} have lower frequencies in BIO-**1** compared to **IBA**.

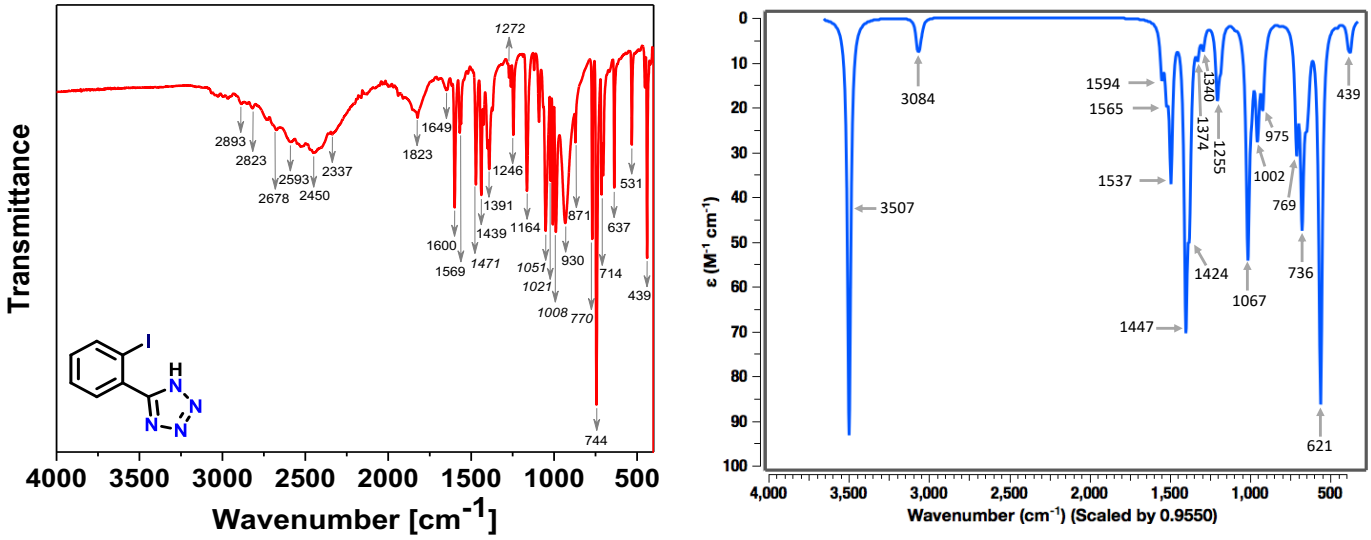

(**a**) (**b**)

Figure 4. (**a**) Experimental, and (**b**) theoretical IR spectra of **IPT**.

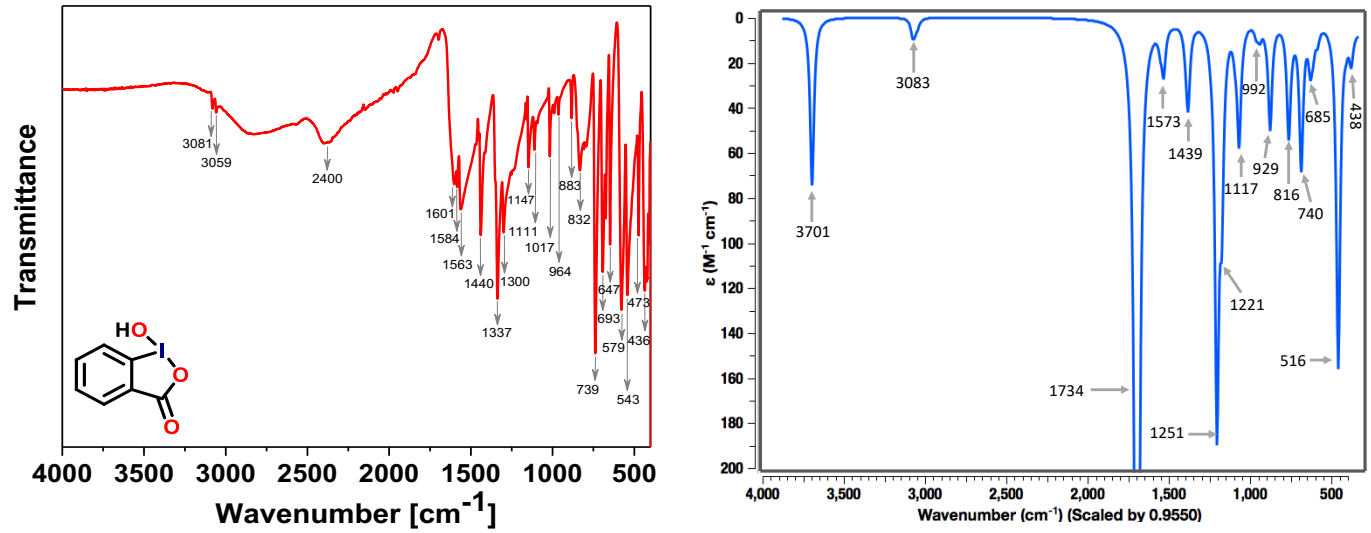

(**a**) (**b**)

Figure 5. (**a**) Experimental and (**b**) theoretical IR spectra of BIO-**1**.

Figure 6a,b show the *exp* and *theor* IR spectra of BIAT-**5**, respectively. The *exp* spectrum has six broad peaks between 3500 and 2400 cm^{-1} and several weak signals between 2400 and 1500 cm^{-1}. There are two signals at 3394 and 3463 cm^{-1} which are not pronounced in the spectrum of **IPT**. The other three peaks at 3062, 2970, and 2901 cm^{-1} are more than 100 cm^{-1} higher than corresponding signals for **IPT**. At 2408 cm^{-1}, there is a single peak, whereas **IPT** has several signals in the same domain. There is an absence of pronounced signals between 1900 and 1500 cm^{-1}, but this domain contains noise which may be significant. There are three weak signals from 1454 to 1377 cm^{-1}, which are almost 20 cm^{-1} lower than the corresponding signals of **IPT**. The *theor* spectrum of BIAT-**5** contains sharp peaks at 3697 and 3085 cm $^{-1}$, with the former having high intensity. The *theor* and *exp* spectra of BIAT-**5** match well, with the exception being the *exp* signal at 2408 cm $^{-1}$, which is not pronounced in the *theor* spectrum. Comparison between *theor* spectra of BIAT-**5** and **IPT** reveals all of the signals between 3697 and 1235 cm $^{-1}$ have higher frequencies in BIAT-**5**, with the peak at 3697 cm^{-1} being 190 cm^{-1} higher compared to the corresponding peak of

IPT. Conversely, between 1235 and 400 cm^{-1}, **IPT** has higher frequencies, the exception being at 738 cm^{-1} in BIAT-**5** and 736 cm^{-1} in **IPT**.

There are significant differences between *exp* and *theor* IR spectra which are mostly attributable to the phase difference in this case, but it is evident that the two can be mapped to one another. LVM analysis not only confirms the accurate mapping of *exp* to *theor* vibrational frequencies, but it also provides a probe of vibrational spectra with a level of detail otherwise unobtainable, as is demonstrated in the following subsection.

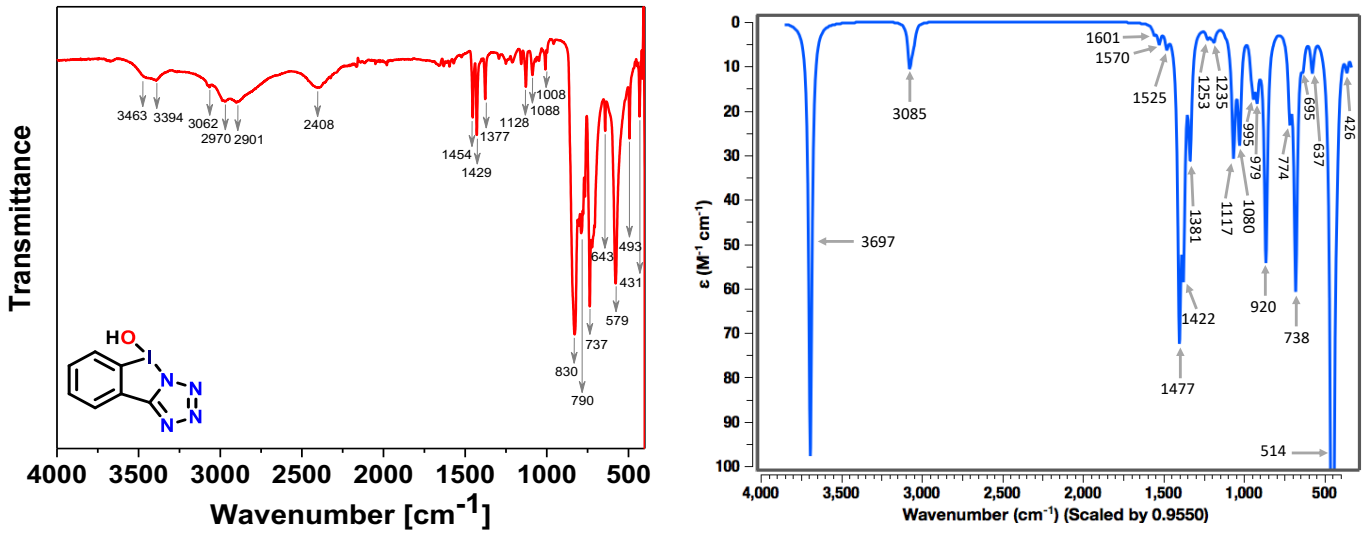

(**a**) (**b**)

Figure 6. (**a**) Experimental and (**b**) theoretical IR spectra of BIAT-**5**.

CNM Analysis

There are many common IR signatures and numerous charts exist to help with assigning functional groups for the most recognizable signals, but doing so neglects the fact that normal vibrational modes are delocalized. In other words, most vibrational frequencies are composed of several molecular motions rather than a single C−C or C−N stretch for example. This is where LVM theory provides valuable new insights for the analysis of vibrational spectra through decomposition of normal vibrational modes into individual LVM contributions from local parameters bond distance (R), angle (θ), and dihedral/torsion (φ).

Figure 7 shows CNM, for **IBA**, including normal mode frequencies 439 through 3507 cm^{-1}. **IBA** has eight normal modes with frequencies below 400 cm^{-1}, but the CNM plots do not include these frequencies in accordance with the *exp* IR spectrum. Most of these eight frequencies are related to the LVMs of iodine, and this is consistent for CNM of **IPT**, BIO-**1**, and BIAT-**5**. In addition, included in Figure 7 is a schematic showing the atom numbers and a legend for the color coding of individual LVM contributions: R, θ, and φ.

There are three highly localized normal modes: (1) 3642 cm^{-1} (3810 cm^{-1} *exp*) which is the pure O−H stretch, (2) 78%, 1752 cm^{-1} (1668 cm^{-1} *exp*) is the C12-O13 carbonyl stretch combined with bending motions of C3-C12/O−C−O, and (3) 576 cm^{-1} (635 cm^{-1} *exp*) is 93% dihedral C3-C12-O14-H15 wagging motion. The normal vibrational mode at 451 cm^{-1} corresponds with the 465 cm^{-1} peak in the *exp* spectrum, and is composed primarily of C3−C12−O13 and C3−C12−O14 bending modes (56%), which consist of the Ar C-atom bound to COOH, both O-atoms, and the COOH C-atom. Vibrations from the bending motions of C3−C4−I11, C3−C12, and C2−C3−C12 account for 17% of this normal mode. C3 (the Ar C-atom) is the only atom included in each of the aforementioned LVMs. Other notable signals are at 733/738 (*theor*/*exp*), 1013/1002, and 1250/1170 cm^{-1}. In addition, 44% of the signal at 1170/1250 cm^{-1} is comprised of the C12-O14-H15 bend—10% and 9% of this mode consist of the C3-C12 stretch and the C12-O14 asymmetric stretch. The signals at 3058, 2972, and 2809 cm^{-1} (3086 cm^{-1} *theor*) are the C−H symmetric stretches.

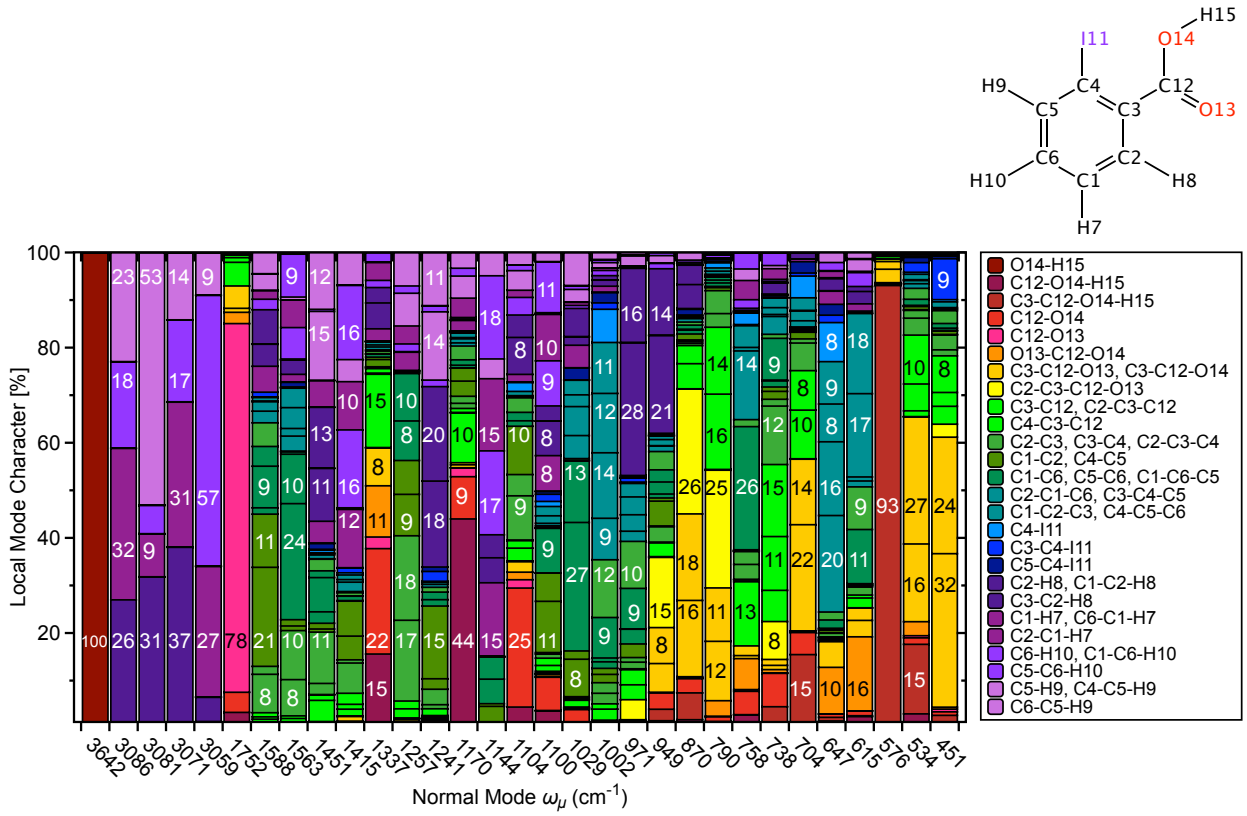

Figure 7. Decomposition of normal vibrational modes into % LVM contributions, also called characterization of normal modes (CNM) for **IBA**; normal vibrational modes 451 through 3642 cm^{-1}. Normal modes below 400 cm^{-1} are excluded to coordinate with experimental IR spectra.

The IR spectra of 5-phenyltetrazole derivatives with various substituents in the phenyl rings, including the spectrum of the *ortho*-iodo derivative, **IPT**, have been reported [138]. Six of the absorption bands in the spectrum of **IPT**, listed as 1467(s), 1269(w), 1048(s), 1018(m), 1005(s), and 767(m) cm^{-1}, were assigned to vibrations of the TZ ring. Each of these bands were also observed in this work (shown in italics in Figure 4a), and are within 3 to 4 cm^{-1} of the previous literature values. The authors in [138] provide an in-depth discussion on the IR spectrum of 5-phenyltetrazole and the combinations of vibrations responsible for the occurrence of all absorption bands are in agreement with the above assignments. For example, the band at 1465 cm^{-1} in the spectrum of 5-phenyltetrazole (likely of similar origin as the band at 1467 (1471 in this work) cm^{-1}) in the spectrum of **IPT** was attributed to a combination of vibrations from C−NH (37%), C=N (36%), N−NH (16%), and N=N (15%). In addition, more complex vibrations involving three atoms, such as N−N=N (12%) and C=N−N (9%), were reported [139]. In the current work, LVM contributions to the frequencies observed in the IR spectrum of **IPT** are discussed in more detail.

Figure 8 is the CNM plot of **IPT**, including normal modes at 439 through 3507 cm^{-1}. The highest *theor* frequency at 3507 cm^{-1} is a pure N−H stretch. This peak is not in the *exp* spectrum, which is likely due to intermolecular hydrogen bonding in the solid phase. No other normal modes for **IPT** contain more than 59% contributions from a single local mode.

Figure 9 is the CNM plot of BIO-**1**, including frequencies spanning 418 through 3701 cm^{-1}. The highest *theor* frequency at 3701 cm^{-1} is a pure N−H stretch; this peak is not pronounced in the *exp* spectrum, which is again attributable to intermolecular HBs in the solid phase. Important LVM contributions are as follows: 3081/3059 (*exp*) $\longrightarrow$ 3093 (*theor*), symmetric *ortho*-C10−H13 and *meta*-C9−H15; 3083 (*theor*), symmetric stretch *meta*-C7−H14, *para*-C8−H12. The other two C−H stretches are asymmetric; 3073, asymmetric stretch of the two *meta*-C−H bonds C7−H14 (*meta*), C9−H15 (*meta*), C8−H12 (*para*),

plus *ortho*-C10-H13; 3061: asymmetric stretch of the two *meta*-C−H bonds *meta*-C7−H14, C9−H15 (*meta*), C8−H12 (*para*).

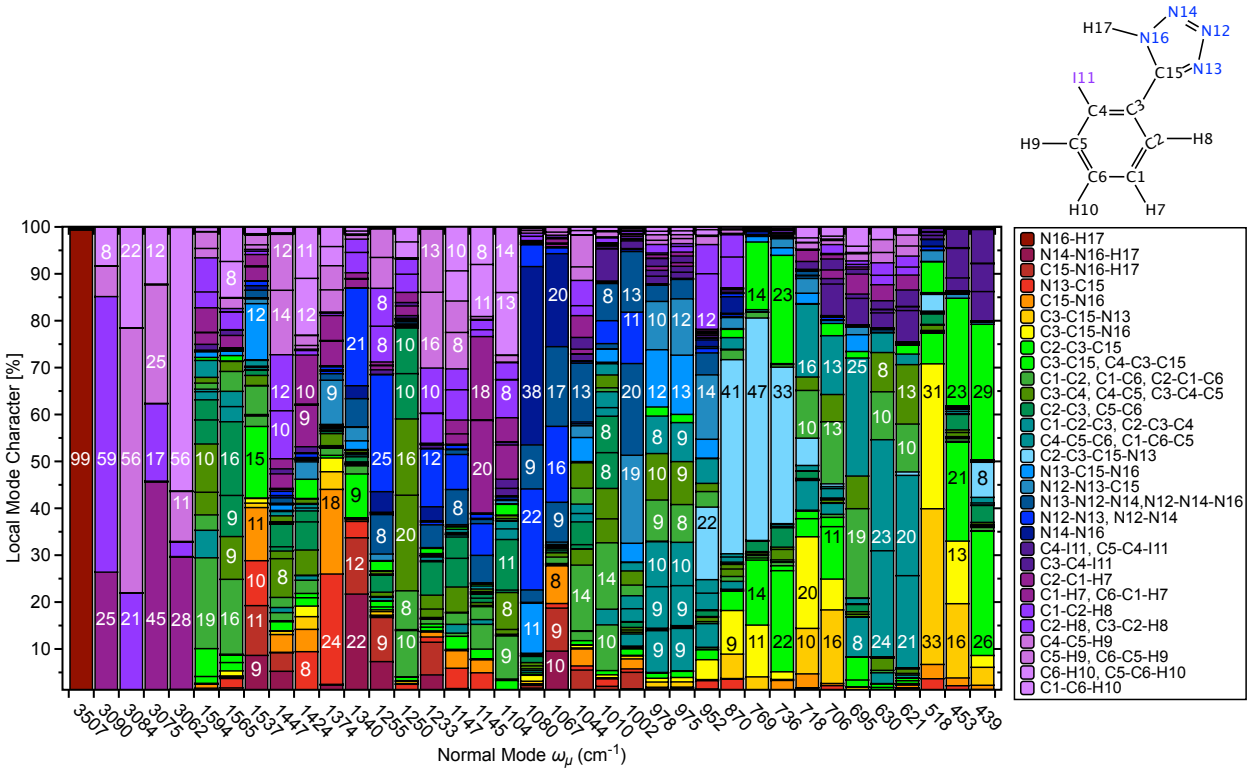

Figure 8. CNM plot of **IPT**; normal vibrational modes in the frequency domain of 439 through 3507 cm^{-1}.

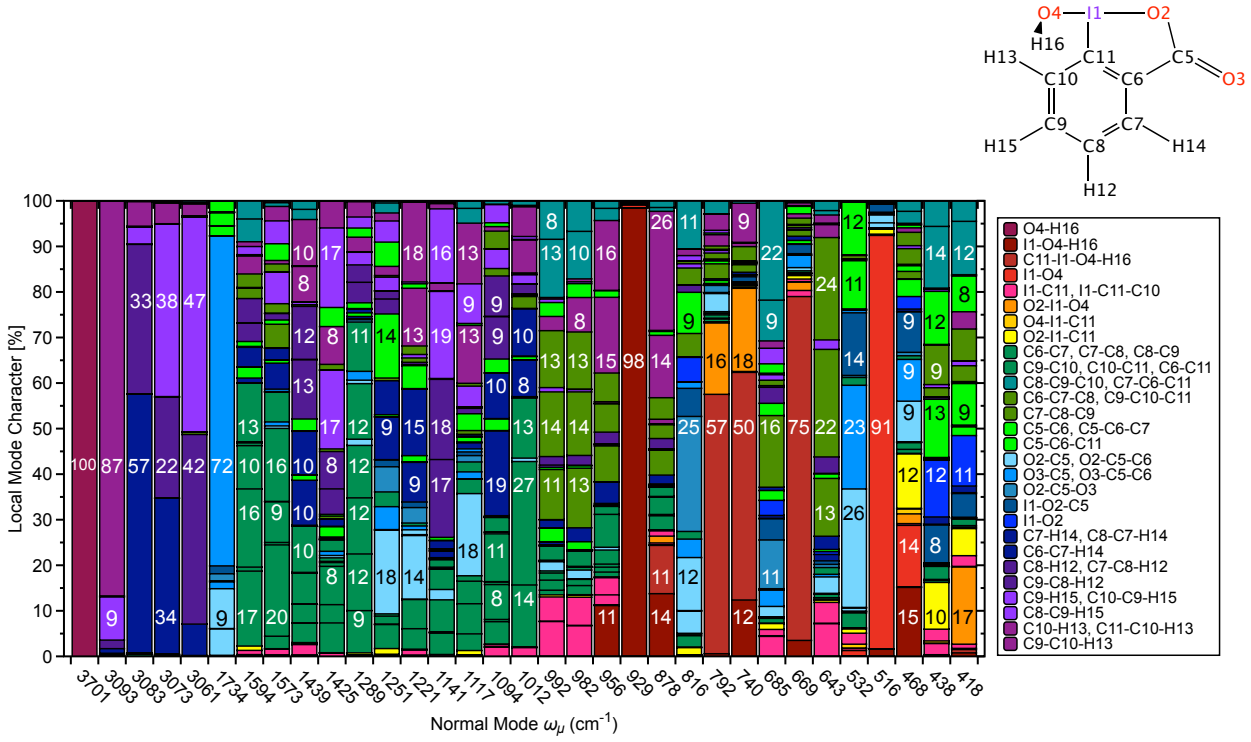

Figure 9. CNM plot of BIO-**1**; normal vibrational modes in the frequency domain of 418 through 3701 cm^{-1}.

Figure 10 is the CNM plot of BIAT-**5**, including normal modes spanning 426 through 3697 cm^{-1}. The *theor* signal at 3697 cm^{-1}, which corresponds with *exp* frequencies of 3463 and 3394 cm^{-1}, is a pure O−H stretch. *Theor* frequencies 3093, 3085, and 3075 cm^{-1} (3062, 2970, 2901 cm^{-1} *exp*) consist entirely of C−H symmetric and asymmetric stretches. The *exp* signal at 2408 cm^{-1} is not pronounced in the *theor* spectrum. The *exp* signal at 1454 cm^{-1} corresponds with the *theor* signal at 1447 cm^{-1}. Motions combined within this mode are: C−H wag (11% *meta*-C10−H16, 10% C12−C10−H16) and C−N asymmetric stretches (17% N3−C13, N4−C13). The remaining 67% of this frequency consists of numerous Ar C−C and C−H stretches, N−C−N angular modes, and C9−C13 bend/C11−C9−C13 angular modes. Each of the aforementioned LVMs contributes < 8%. The *theor* signal at 1381 cm^{-1} (1377 cm^{-1} *exp*) corresponds with N3−C13 stretch (26%) and N4−C13 bend (7%), 8% N2−N3−C13, and 30% *ortho*-C8−H15/*meta*-C10−H16/*para*-C12−H18 bends including C−C−H. 1117 (1128 *exp*) cm^{-1} consists primarily of N−N asymmetric stretches (47%) and N−N−N angular mode (46%). The signal at 920 cm^{-1} (830 *exp*) is a pure I1−O6−H14 bend. The normal mode at 738 cm^{-1} (737 *exp*) is 14% I1−O6−H14 and 76% O6−I1−C7−C8, and at 514 (579 *exp*) cm^{-1} is 93% I1−O6 and 426 (431 *exp*) is 94% O6−I1−C7−C8 torsion. The normal modes at 426, 514, 517, and 695 through 920 cm^{-1} mainly consist of the various LVMs associated with iodine. The N−N and N−N−N LVMs are mostly contained within normal modes 995, 1080, and 1117 cm^{-1}.

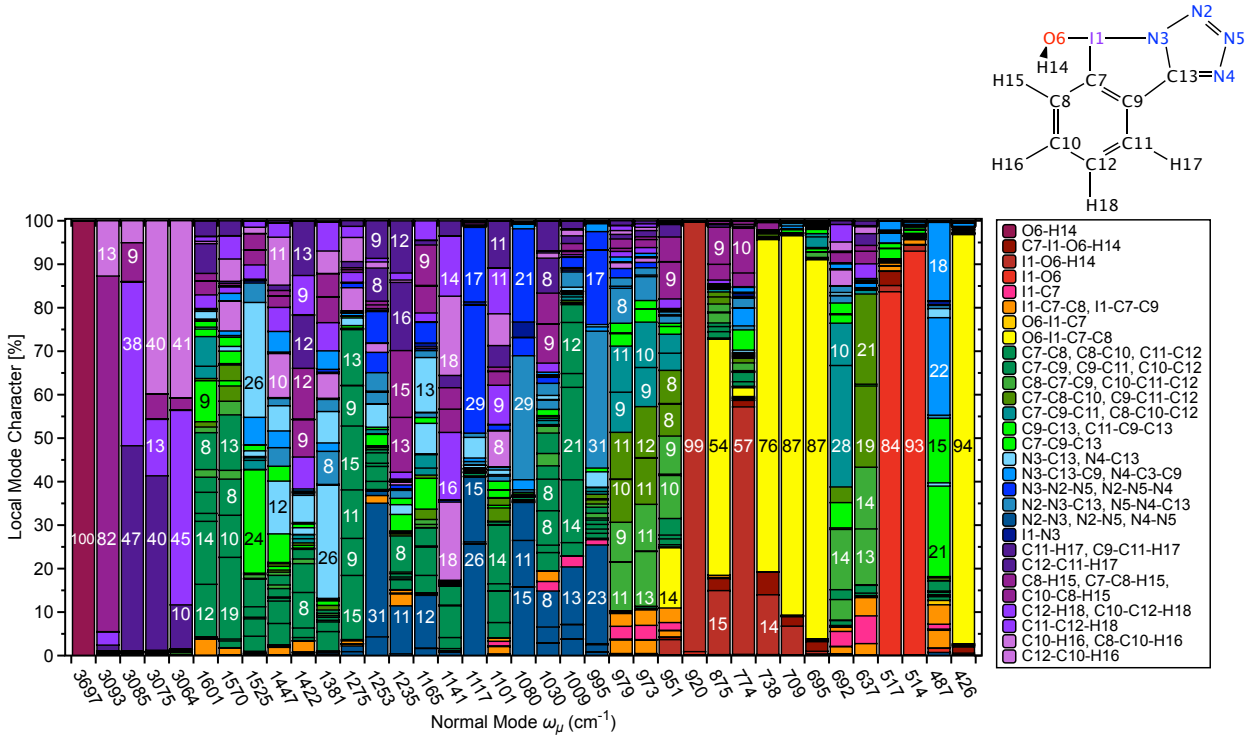

Figure 10. CNM plot of BIAT-**5**; normal vibrational modes in the frequency domain of 426 through 3697 cm^{-1}.

3.2. NBO Analysis

In Figure 1, atomic and group NBO charges for all molecules (reference systems **IBA** and **IPT**, BIOs **1–4**, and BIATs **5–8**) investigated in this work are reported (see also Table 3). NBO atomic charges of iodine are shown in purple, carbon in black, oxygen in red, and nitrogen in blue. Figure 1 also shows the total NBO charge of the Ar group in black, the TZ group in blue, and the alkoxy group in red. The iodine-atomic NBO charge in **IBA** is slightly more positive compared to **IPT** (0.179 and 0.158 *e*, respectively) and the total charge of the Ar group in **IBA** is significantly more negative compared to **IPT** (−0.213 and −0.126 *e*, respectively); while the total charges of COOH in **IBA** and TZ in **IPT** are

both close to zero, with COOH having a net positive charge (0.035 *e*) and TZ having a net negative charge (−0.032 *e*).

Comparing NBO charges of **IBA** with those of **IPT** reveals some significant electronic differences which extend to BIOs **1–4** and BIATs **5–8**, namely the following: charge (and electronic density) distribution are more polar in **IBA** compared to **IPT**, and NBO charge/electronic density is significantly higher/more negative on the Ar ring in **IBA** compared to **IPT**. On the other hand, in **IPT**, more electron density is transferred to TZ, which becomes more negative relative to the total COOH charge in **IBA**, showing a stronger electron withdrawing effect of the TZ group. It is also interesting to note that the presence of the TZ group in **IPT** increases the electron density/negative charge on the Ar-carbon atom bound to iodine relative to that of **IBA** (NBO charges of −0.133 and −0.129 *e*, respectively). Consequently, iodine is less positive in **IPT** compared to **IBA** (NBO charge values of 0.158 and 0.179 *e*, respectively).

To reiterate some of the aforementioned observations, **1–8** show similar trends in charge and electron density distribution with respect to the comparison of **IBA** and **IPT**. The iodine-atomic charge in BIO-**1** is slightly more positive compared to BIAT-**5** (1.329 and 1.294 *e*, respectively), the charge of the Ar group is significantly more negative (−0.224 *e* BIO and −0.120 *e* BIAT, respectively), and the charge on TZ in **5** is more negative than COO^- in **1** (−0.639 and −0.569 *e*, respectively). However, in contrast with **IBA** and **IPT**, the Ar-C atomic charge (bound to iodine) in **1** is slightly more negative relative to **5** (−0.195 and −0.178 *e*, respectively). COO^- groups in BIOs **2–4** show similar charge differences compared with TZ groups in BIATs **6**, **7**, and **8**, which show a similar increase in electron withdrawing abilities of the TZ groups in the BIATs, as was observed in **IPT**.

The electron withdrawing ability of the TZ groups in BIATs **5–8** increases in series, as the charges of these groups become more negative (−0.639, −0.642, −0.644, and −0.648 *e*, respectively), which correlates to more negative charges on the Ar groups (−0.120, −0.125, −0.128, and −0.130 *e*, respectively). A methyl group is a stronger σ-electron donor than H, and the increasing number of methyl substituents in the alkoxy groups MeO ⟶ EtO ⟶ iPrO increases electron density transfer to the Ar and TZ groups in series. This causes increased negative charges, despite the fact that both the TZ and the Ar groups are not directly bound to the alkoxy groups. It is also interesting to note that, in the same series, the charge on iodine becomes more positive (1.294, 1.302, 1.307, and 1.308 *e*, respectively). A similar trend is observed for BIOs **1**–**4**. Increasing the number of carbon atoms in the alkoxy groups results in increasingly more negative charges on the COO^- groups (−0.569, −0.571, −0.573, and −0.575 *e*, respectively), and the Ar groups (−0.224, −0.228, −0.231, and −0.232 *e*, respectively), while the iodine-atomic charges become more positive (1.329, 1.336, 1.341, and 1.343 *e*, respectively). The iodine atoms in this case, similar to I_2, show both σ-electron donor and acceptor capabilities [140]. In addition to the special properties of HVI, iodine can form an efficient bridge between molecular groups of different electron donor/acceptor abilities.

NBO charges of the hydroxyl/alkoxy O-atoms vary significantly in series for BIOs **1–4** (−1.003, −0.786, −0.795, −0.802 *e*, respectively), whereas the combined charge of the whole functional group only varies by 0.002 *e* in the same series. Likewise, for BIATs **5–8**, O-atomic charges vary by 0.216 *e*, whereas hydroxyl/alkoxy group charges vary by 0.004 *e*. The I-atomic charge becomes more positive in the same series, i.e., the I-atomic charge increases in magnitude as the mass of the hydroxyl/alkoxy group increases. NBO charge of the Ar rings become slightly more negative in the same series (−0.224 to −0.232 *e* in BIOs **1–4** and −0.120 to −0.130 *e* in BIATs **5–8**, respectively). With the exception of the hydroxyl/alkoxy O-atoms, the difference in atomic NBO charges between O, N, and C-atoms bound to iodine remains relatively constant. The NBO charge on iodine varies, but to a lesser extent compared to he hydroxyl/alkoxy O-atoms; Δ NBO = 0.014 *e* and 0.218 *e*, respectively. Generally, more insights into the differences in electronic structure, density, and populations are obtained by considering the net NBO charge of the entire functional group rather than the charge on the atom which bonds directly to iodine.

Table 3. Theoretical bond lengths R (Å), local mode vibrational force constants k^a (mDyn/Å), local mode vibrational frequencies ω^a (cm^{-1}), electronic densities at the bond critical points $\rho(\mathbf{r}_b)$ (e/Å^3), energy densities at the bond critical points $H(\mathbf{r}_b)$ (Hartree/Å^3), and atomic NBO charges (e) for all I−C, I−N, and I−O bonds in **IBA**, **IPT**, and **1–8**, calculated at the ωB97X-D/Def2-TZVP level of theory.

#	Bond	R	k^a	ω^a	$\rho(\mathbf{r}_b)$	$H(\mathbf{r}_b)$	Atom	Charge
IBA	I−C4	2.097	2.536	626.6	0.887	−0.488	C4	−0.199
	-	-	-	-	-	-	I	+0.179
IPT	I−C4	2.102	2.468	618.1	0.881	−0.482	C4	−0.134
	-	-	-	-	-	-	I	+0.158
1	I−O2	2.121	1.671	446.8	0.679	−0.276	O2	−0.740
	I−O4	2.009	2.472	543.4	0.862	−0.425	O4	−1.003
	I−C	2.092	2.615	636.3	0.939	−0.544	C11	−0.195
	-	-	-	-	-	-	I	+1.329
2	I−O2	2.125	1.609	438.4	0.675	−0.273	O2	−0.740
	I−O4	2.002	2.442	540.1	0.880	−0.442	O4	−0.786
	I−C	2.093	2.590	633.2	0.937	−0.542	C11	−0.195
	-	-	-	-	-	-	I	+1.336
3	I−O2	2.128	1.575	433.8	0.671	−0.270	O2	−0.741
	I−O4	1.999	2.462	542.4	0.885	−0.446	O4	−0.795
	I−C	2.093	2.586	632.7	0.937	−0.542	C11	−0.195
	-	-	-	-	-	-	I	+1.341
4	I−O2	2.131	1.552	430.6	0.666	−0.266	O2	−0.742
	I−O4	1.998	2.459	542.1	0.884	−0.444	O4	−0.802
	I−C	2.093	2.574	631.3	0.936	−0.540	C11	−0.194
	-	-	-	-	-	-	I	+1.343
5	I−N	2.204	1.389	432.3	0.636	−0.246	N3	−0.424
	I−O	2.010	2.434	539.2	0.862	−0.425	O6	−1.004
	I−C	2.117	2.378	606.8	0.904	−0.504	C7	−0.178
	-	-	-	-	-	-	I	+1.294
6	I−N	2.209	1.333	428.5	0.630	−0.241	N3	−0.423
	I−O	2.002	2.410	533.4	0.881	−0.443	O6	−0.788
	I−C	2.117	2.360	603.9	0.902	−0.502	C7	−0.178
	-	-	-	-	-	-	I	+1.302
7	I−N	2.213	1.325	422.3	0.624	−0.237	N3	−0.423
	I−O	1.999	2.437	539.7	0.887	−0.447	O6	−0.797
	I−C	2.117	2.371	605.9	0.903	−0.503	C7	−0.178
	-	-	-	-	-	-	I	+1.307
8	I−N	2.218	1.307	419.5	0.617	−0.232	N3	−0.423
	I−O	1.998	2.442	540.2	0.887	−0.446	O6	−0.804
	I−C	2.118	2.370	605.7	0.901	−0.501	C7	−0.178
	-	-	-	-	-	-	I	+1.308

Most notable is the difference in NBO charges of the whole Ar rings between BIOs and BIATs. For the BIOs, Ar NBO charges are more negative compared to BIATs by up to 0.104 e (60.5% difference). On the other hand, BIAT TZ group charges are more negative compared to BIO OCO group charges by up to 0.079 e. This is a result of the ability of TZs, particularly pronounced in amino-TZs to withdraw electrons [141–143]. Iodine can also accept an electronic charge from an Ar ring through a σ-hole interaction. However, given the abundance of lone pairs electrons (lp) in iodine and comparatively low electronegativity, iodine is as likely to be an electron donor as it is an acceptor. This result seems subtle, but it points to the C−C bond between TZ/OCO and Ar as a channel for the transfer of negative charge from the latter to the former. This finding naturally draws interest in the LVMs

as well as electronic density ($\rho(\mathbf{r}_b)$) of this connecting C−C bond. The importance of this connector C−C bond is addressed in the following subsection.

3.3. LVM and QTAIM Analyses

Table 3 depicts chemical bond strength of all iodine-containing bonds: I−C, I−N, and I−O, expressed as LVM stretching force constants k^a, along with ionic character described by the local energy density $H(\mathbf{r}_b)$. In Figure 11a,b, k^a of all I−N, I−O, and I−C bonds are plotted with respect to bond length R (Figure 11a) and $H(\mathbf{r}_b)$ (Figure 11b). Generally, increase in bond strength roughly correlates with shorter R and increase in covalent character of the bond ($H(\mathbf{r}_b)$ values increasing in magnitude). The I−C and I−OR bonds are significantly stronger than the I−N and the I−O (CO) bonds. The I−C bonds are approximately 0.1 Å longer than the I−OR bonds, but are similar in strength. All eight I−OR bonds are with in 0.06 mDyn/Å of each other. The ten I−C bonds show the following trend in terms of bond strength: BIOs **1–4** > **IBA** > **IPT** > BIATs **5–8**. The I−N bonds are slightly weaker than the I−O (CO) bonds, and bond strength decreases in series (i.e., bond strength decreases as size of OR increases).

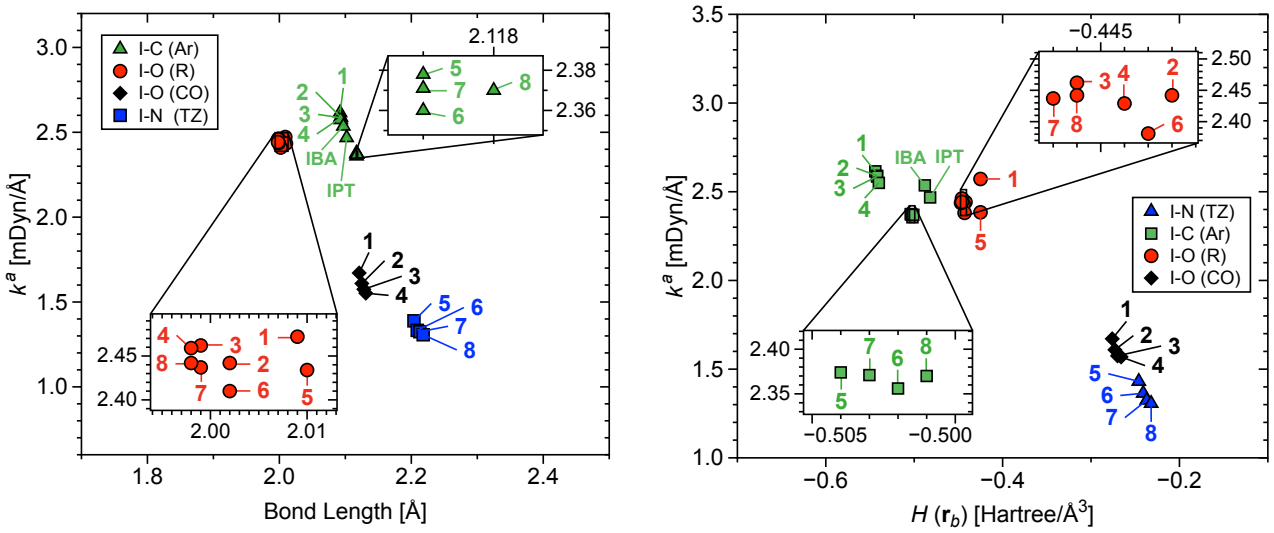

Figure 11. Local mode vibrational force constant k^a plotted with respect to (**a**) R, and (**b**) $H(\mathbf{r}_b)$ of iodine-based bonds for structures **1–8**.

In Figure 12a,b, k^a of all I−N, I−O, and I−C bonds are plotted with respect to electronic density at the bond critical point (BCP) $\rho(\mathbf{r}_b)$ (Figure 12a) and angle θ of the L−I−L 3c-4e bonds (Figure 12b). Similar to the trend of $H(\mathbf{r}_b)$, electron density increases with increasing bond strength. The I−N bonds have the lowest electron densities at the BCPs, and the I−C bonds of BIOs **1–4** have the most electron density at the BCPs. Increase in angle θ of the 3c-4e bond roughly correlates with increasing bond strength. This correlation is strongest for the I−N and I−O (CO) bonds. Interestingly, even though the I−C bonds of BIOs **1–4** are perpendicular to the 3c-4e bonds, increasing the O−I−O angle roughly translates to increase in I−C bond strength. This indicates that a more linear 3c-4e bond allows for better orbital overlap and more electronic density at the equatorial positions around iodine. In addition, it is notable that the 3c-4e bond angles in the BIATs are approximately 2.5° smaller compared to the BIOs.

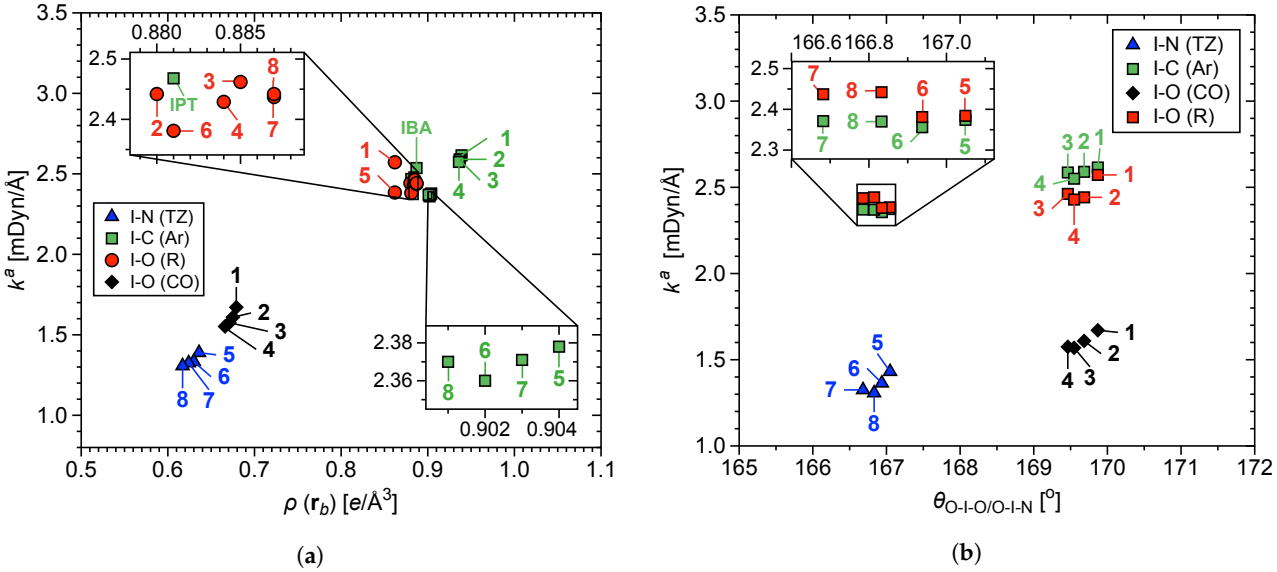

(**a**) (**b**)

Figure 12. Local vibrational mode stretching force constant k^a of all iodine-based bonds (three per compound) plotted with respect to (**a**) $\rho(\mathbf{r}_b)$, and (**b**) bond angle θ of O−I−O (**1–4**) and O−I−N (**5–8**) axial−I−axial 3c-4e interactions.

Figure 13a,b show local vibrational force constants of the iodine-related bonds plotted against the difference of the NBO charges between the two bonding atoms. There is a linear correlation between Δ NBO charge and force constant for the I−N (TZ) and the I−O (OCO) bonds, with the stronger bonds having smaller Δ NBO charges. Compared to the BIOs, the BIATs have weaker iodine-related bonds and larger Δ NBO values. For the I−C bonds, there is a similar trend, but it is extremely subtle. There is no such correlation for the I−O (hydroxyl/alkoxy) bonds.

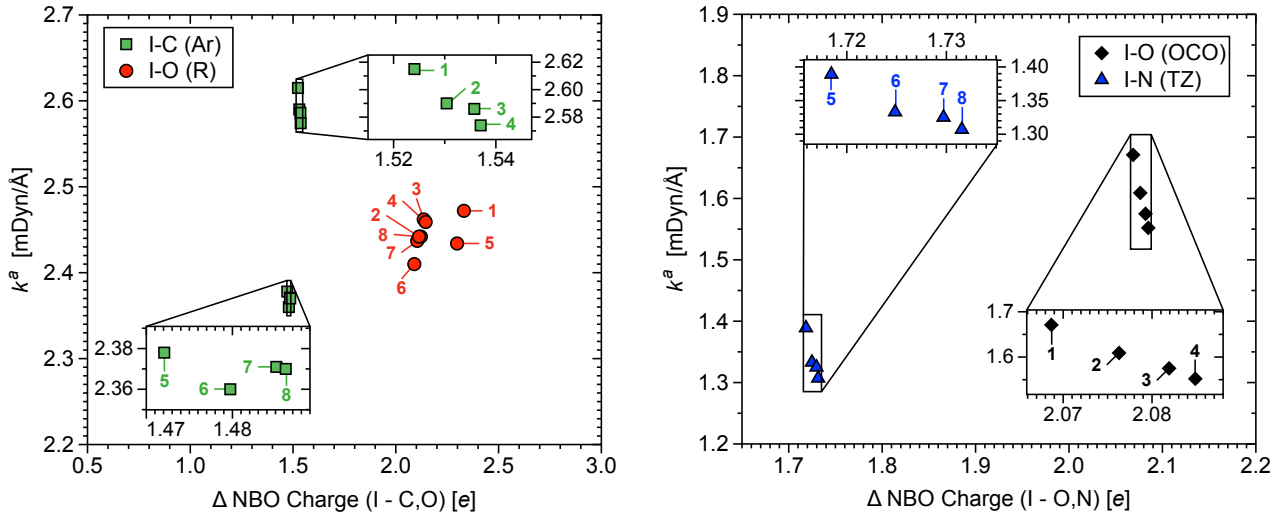

(**a**) (**b**)

Figure 13. Local mode vibrational force constant k^a of iodine-related bonds plotted with respect to Δ NBO charge between the bonding atoms (**a**) I−C (Ar) and I−O hydroxyl/alkoxy (R), and (**b**) I−N and I−O (OCO).

For BIOs **1–4**, strength of the I−C bond decreases in series (k^a = 2.615, 2.590, 2.586, and 2.550 mDyn/Å, respectively), the energy density decreases almost in series (the $H(\mathbf{r}_b)$ value of −0.544, −0.542, −0.542, and −0.540 Hartree/Å^3, respectively), and the charge difference increases in series (Δ NBO values of 1.524, 1.531, 1.536, and 1.538 e, respectively). In other words, the I−C bond in this series becomes weaker, less covalent, with increased polarization of the electron density. Strength of the I−O (hydroxyl/alkoxy)

bonds do not follow the trend of the I−C bonds, with k^a values of 2.572, 2.442, 2.462, and 2.459 mDyn/Å, respectively (I−OH > I−OEt > I−OiPr > I−OMe), $H(\mathbf{r}_b)$ values of −0.425, −0.442, −0.446, and −0.444 Hartree/Å^3, respectively (I−OEt > I−OiPr > I−OMe > I−OH), and Δ NBO values of 2.332, 2.122, 2.136, and 2.138 *e*, respectively (I−OH > I−OiPr > I−OEt >I−OMe). To summarize some rather surprising results for the I−O (hydroxyl/alkoxy) bonds, the I−OH bond is the strongest but has the lowest energy density, the I−OiPr bond is weaker than the I−OEt bond, and the I−OMe bond is the weakest of the four bonds. Excluding the I−N bonds of BIATs **5–8**, the I−OCO bonds between iodine and the carboxylate ester group in BIOs **1–4** are the weakest of the iodine-related bonds (k^a values of 1.671, 1.609, 1.575, and 1.569 mDyn/Å, respectively), the energy density decreases in magnitude in series ($H(\mathbf{r}_b)$ values of −0.276, −0.273, −0.270, and −0.266 Hartree/Å^3, respectively), and the charge difference increases (Δ NBO values 2.069, 2.076, 2.082, and 2.085 *e*, respectively). These changes indicate that the I−OCO bond becomes weaker with less covalent character and larger more polarized electron density.

For BIATs **5–8**, the I−C bond strength varies unpredictably (k^a values of 2.374, 2.356, 2.371, and 2.370 mDyn/Å, respectively), as does energy density ($H(\mathbf{r}_b)$ values of −0.504, −0.502, −0.503, and −0.501 Hartree/Å^3, respectively), but the charge difference increases in series (Δ NBO values of 1.472, 1.480, 1.485, and 1.486 *e*, respectively). This indicates that the polar character of the I−C bond increases in the same series. In BIAT-**5**, I−OH bond strength is slightly stronger than the I−OMe bond in BIAT-**6** (+0.003 mDyn/Å), but generally bond strength increases in series (k^a values of 2.384, 2.381, 2.437, and 2.442 mDyn/Å, respectively). Energy density is 0.001 Hartree/Å^3 larger for BIAT-**7** compared to BIAT-**8**, but generally increases in magnitude in series ($H(\mathbf{r}_b)$ values of −0.425, −0.443, −0.447, and −0.446 Hartree/Å^3, respectively), and the I−OH bond of BIAT-**5** is the most polar but charge difference increases in series for the three I−O (alkoxy) bonds (Δ NBO values of 2.298, 2.090, 2.104, and 2.112 *e*, respectively), showing that the I−O (alkoxy) bond becomes stronger, more covalent, and less polarized. Bond strength of I−N in BIATs **5–8** decreases in series (k^a values of 1.431, 1.364, 1.325, and 1.307 mDyn/Å, respectively), the energy density decreases in series ($H(\mathbf{r}_b)$ values of −0.246, −0.241, −0.237, and −0.232 Hartree/Å^3, respectively), and the charge difference increases in series (Δ NBO values of 1.718, 1.725, 1.730, and 1.731 *e*, respectively),

Table 4 summarizes LVM, QTAIM, and NBO results for the C−C bonds which link Ar and OCO/TZ groups in **IBA**, **IPT**, BIOs **1–4**, and BIATs **5–8**. In addition to the I−N bonds, this bridging C−C bond is a potential weak point, as well as a location for electron transfer. These C−C bonds are significantly stronger than the iodine-related bonds but are significantly weaker than the C−C, C−O, C−N, and N−N bonds. According to Table 4, the C−C bond is stronger for **IPT** compared to **IBA** (the k^a values of 4.468 and 4.408 mDyn/Å, respectively), is shorter (R values of 1.469 and 1.495 Å, respectively), and has a more covalent character (the $H(\mathbf{r}_b)$ values of −1.782 and −1.688 Hartree/Å^3). The difference between the NBO charges of both C atoms in this bond for **IPT** is smaller compared to **IBA** (Δ NBO values of 0.4368 and 0.9691 *e*, respectively), which indicates less polarization of this bond in **IPT** and is consistent with larger covalent character [144]. The chemical differences of the C−C bonds in **IPT** and **IBA** is explained by more π-electron delocalization in the TZ group of **IPT**, which leads to a less positive charge of the TZ-carbon compared to the OCO-carbon atom of **IBA** (NBO charge values are 0.3025 and 0.7700 *e*, respectively), resulting in the C−C bond in **IPT** being less polar but stronger. Similar correlations are observed in calculations for BIOs **1–4** and BIATs **5–8**. The C−C bonds in BIATs **5–8** are generally stronger, shorter, and have more covalent character (correlating with a less polar bond) compared to BIOs **1–4**, and the TZ-carbon atoms have less positive NBO charges in contrast with the OCO-carbon atoms. It is also interesting to note that the C−C 'bridge' bond in BIAT-**5** is much stronger than that of **IPT**, where both systems have TZ groups (k^a values of 5.587 and 4.468 mDyn/Å, respectively), thus indicating more π-electron delocalization in **5**. This is corroborated by the TZ-carbon atom charge in BIAT-**5** less positive compared with the **IPT**-carbon atom (NBO charges of 0.2483 and 0.3025 *e*,

respectively), and the bridging C−C bond being less polar in BIAT-**5** compared with **IPT** (Δ NBO values of 0.3509 and 0.4368 e, respectively). The analogous C−C bonds in BIATs **6–8** are very similar to BIAT-**5** in terms of all of the aforementioned properties, indicating that formation of the I−N bond in the BIATs increases the π electron delocalization in the TZ group, making these C−C bonds stronger.

Table 4. Theoretical R (Å), k^a (mDyn/Å), ω^a (cm^{-1}), $\rho(\mathbf{r}_b)$ ($e/Å^3$), $H(\mathbf{r}_b)$ (Hartree/$Å^3$), and NBO atomic charges (e) for the C−C bonds linking Ar groups and TZ/OCO groups in **IBA**, **IPT**, and BIOs/BIATS **1–8**.

#	R	k^a	ω^a	$\rho(\mathbf{r}_b)$	$H(\mathbf{r}_b)$	Atom	Charge	Atom	Charge	Δ Charge
IBA	1.4950	4.408	626.6	1.8291	−1.6880	C12 (OCO)	0.7700	C3 (Ar)	−0.1991	0.9691
IPT	1.4690	4.468	618.1	1.8679	−1.7820	C15 (TZ)	0.3025	C3 (Ar)	−0.1343	0.4368
1	1.5033	4.123	1080.0	1.7951	−1.6272	C5 (OCO)	0.7478	C6 (Ar)	−0.1903	0.9380
2	1.5037	4.120	1079.6	1.7935	−1.6246	C5 (OCO)	0.7482	C6 (Ar)	−0.1902	0.9385
3	1.5042	4.104	1077.4	1.7920	−1.6222	C5 (OCO)	0.7486	C6 (Ar)	−0.1897	0.9382
4	1.5042	4.109	1078.1	1.7920	−1.6222	C5 (OCO)	0.7484	C6 (Ar)	−0.1891	0.9375
5	1.4489	5.587	1257.1	1.9489	−1.9120	C13 (TZ)	0.2483	C9 (Ar)	−0.1026	0.3509
6	1.4489	5.579	1256.2	1.9487	−1.9116	C8 (TZ)	0.2467	C4 (Ar)	−0.1023	0.3490
7	1.4488	5.588	1257.3	1.9486	−1.9114	C13 (TZ)	0.2459	C9 (Ar)	−0.1019	0.3477
8	1.4489	5.583	1256.7	1.9494	−1.9127	C12 (TZ)	0.2448	C8 (Ar)	−0.1012	0.3461

4. Conclusions and Outlook

There are fundamental differences between *exp* and *theor* IR spectroscopy which are mostly attributable to the phase difference in this case, but it is evident that the two can be mapped to one another with relative ease if corrections to the harmonic approximation are considered. LVM analysis not only confirms the accurate mapping of *exp* to *theor* vibrational frequencies, but opens the door to the analysis of vibrational spectra at a level of detail and accuracy not previously known. This work demonstrates the importance of the often overlooked fact that normal vibrational modes are delocalized. LVM theory takes this into consideration, and reveals valuable new insights by decomposing normal vibrational modes into fundamental LVM contributions in terms of R, θ, and φ.

The sensitivity of LVM stretching force constants has also revealed subtle but important differences in the intrinsic nature of iodine-related bonds between a set of four alkoxybenziodoxoles, which are relatively stable, and four tetrazolated derivatives which decompose explosively. The I−N bonds in BIATs **5–8** are generally weaker than the comparable I−OCO bonds in BIOs **1–4** by as much as 0.300 mDyn/Å. Moreover, strength of the I−N bond in BIATs **5–8** decreases with the increasing size of the hydroxyl/alkoxy group: OH > MeO > EtO > iPrO. Based on LVM analysis, I−N is most likely the trigger bond responsible for initiation of explosive decomposition in BIATs **5–8**. For comparison, trigger bonds were recently identified as C−N bonds in the high-energy compounds 1-fluoro-2,4,6-trinitrobenzene and 2,4,6-trinitrobenzaldehyde [31]. Our calculations predict the C−C bond linking Ar and aldehyde groups to be the weakest in the latter, but both bonds in question have k^a values between 3.400 and 3.900 mDyn/Å, whereas the possible I−N trigger bonds, I−C, and I−O bonds in this work have k^a values between 1.300 and 2.620 mDyn/Å. With regard to the I−N bonds, it is interesting to note that explosive compounds with I−N bonds have been known as long as elemental iodine itself. The formation of the highly friction-sensitive black compound NI_3 (or more precisely, its adduct with ammonia), achieved by mixing iodine with aqueous ammonia, was first reported by Bernard Courtois in 1813 in the paper where the discovery of the new element was announced [145]. The composition of the unstable compound was confirmed as $NI_3 \cdot NH_3$ in 1903 [146]. Based on strength of the I−C, I−N, and I−O bonds, where stronger bonds will correlate with increase in stability, we predict stability of BIATs **5–8** as follows: BIAT-**8** < BIAT-**7** < BIAT-**6** < BIAT-**5**. The finer details obtained from this work regarding the characteristics of iodine-containing bonds can lead to new structure–property relationships. Some additional key differences between the BIOs **1–4** and BIATs **5–8** are as follows:

- The TZ groups in BIATs **5–8** are more capable electron withdrawing groups compared to the OCO groups in BIOs **1–4**
- Compared to BIATs **5–8**, BIOs **1–4** have Ar rings nearly two times more negative in charge, iodine atoms with positive in charges, and stronger I−C and I−O (hydroxyl/alkoxy) bonds
- The weakest bonds in this work are the I−N bonds
- The 3c-4e L−I−L bond angles of BIATs **5–8** are up to 2.5° larger compared to the analogous bonds in BIOs **1–4**

Future goals are to investigate the effects other types of substituents will have on the physical properties of benziodazolotetrazoles, which encompasses modifications to the TZ group as well as the Ar group. Furthermore, we plan to investigate the mechanism of detonation using the Unified Reaction Valley Approach to reveal in what order the most important changes in electronic structure occur and determine the most prevalent reaction products. Lastly, we wish to investigate and develop better methods for approximating the anharmonic nature of vibrational frequencies.

Supplementary Materials: The following are available at https://www.mdpi.com/article/10.3390/physchem1010004/s1, Single Crystal X-ray Crystallography data of *I*-hydroxybenziodoxolone (BIO-**1**) including refinement details; Figure S1: Displacement ellipsoid plot (50% probability level) of (BIO-**1**) at 100.0(3) K; Table S1: Crystal data and structure refinement; Table S2: Fractional Atomic Coordinates and Equivalent Isotropic Displacement Parameters; Table S3: Anisotropic Displacement Parameters; Table S4: Bond length; Table S5: Bond Angles; Table S6: Torsion Angles; Table S7: Hydrogen Atom Coordinates.

Author Contributions: Conceptualization, E.K., N.V.T., and S.Y.; methodology, E.K., K.D.S., N.V.T., M.F., and S.Y.; validation, S.Y., M.F., and K.D.S.; formal analysis, S.Y., M.F., and K.D.S.; resources, E.K. and N.V.T.; writing—original draft preparation, S.Y. and E.K.; writing—review and editing, E.K., S.Y., M.F., K.D.S., and N.V.T.; visualization, S.Y., M.F., and K.D.S.; supervision, E.K. and N.V.T.; funding acquisition, E.K. and N.V.T. All authors have read and agreed to the published version of the manuscript.

Funding: This research was funded by the National Science Foundation Grant Nos. CHE-1464906 (E.K.) and CHE-1455200 (N.V.T.).

Acknowledgments: The authors thank SMU for generously providing computational resources and analytical instrumentation and Daniel Unruh of Texas Tech University for collection and analysis of the X-ray diffraction data. This work was completed while N.V.T. was serving at the National Science Foundation, and the support of the Foundation is gratefully acknowledged.

Conflicts of Interest: The authors declare no conflict of interest.

Abbreviations

The following abbreviations are used in this manuscript:

3c-4e	3-Center 4-Electron
Ar	*Ortho*-Disubstituted Benzene
BIAT	Benziodazolotetrazole
BIO	Alkoxybenziodoxole
CNM	Characterization of Normal Modes
CT	Charge Transfer
DFT	Density Functional Theory
exp	Experimental
HV	Hypervalent
HVI	Hypervalent Iodine

IBA	2-Iodobenzoic Acid
IPT	5-(2-Iodophenyl)tetrazole
L	Ligand
LVM	Local Vibrational Mode
MAE	Mean Absolute Error
NBO	Natural Bond Orbital
OCO	Carboxyl/Carboxylate Ester
RCN_4^-	Tetrazolate
RCO_2^-	Carboxylate
RMSE	Root Mean Square Error
theor	Theoretical
TZ	Tetrazole

References

1. Varvoglis, A. *Organic Compounds of Polycoordinated Iodine*; Wiley-VCH: Weinheim, Germany, 1992; p. 414, ISBN 0471188255.
2. Willgerodt, C. *Die Organischen Verbindungen mit Mehrwertigem Jod*; Ferdinand Enke: Stuttgart, Germany, 1914; p. 266, ISBN 978-0526136322.
3. Varvoglis, A. *Hypervalent Iodine in Organic Synthesis*; Academic Press: San Diego, CA, USA, 1997; p. 223, ISBN 0-12-714975-9.
4. Wirth, T. *Hypervalent Iodine Chemistry: Modern Developments in Organic Synthesis*; Springer: Berlin, Germany, 2003; p. 264, ISBN 978-3-540-44107-6.
5. Zhdankin, V.V. *Hypervalent Iodine Chemistry: Preparation, Structure and Synthetic Applications of Polyvalent Iodine Compounds*; Wiley: Chichester, UK, 2014; p. 468, ISBN 9781118341032.
6. Yoshimura, A.; Zhdankin, V.V. Advances in Synthetic Applications of Hypervalent Iodine Compounds. *Chem. Rev.* **2016**, *116*, 3328-3435. [CrossRef] [PubMed]
7. Zhdankin, V.V. Hypervalent iodine compounds: Reagents of the future. *Arkivoc* **2020**, *iv*, 1–11. [CrossRef]
8. Zhdankin, V.V. Benziodoxole-Based Hypervalent Iodine Reagents in Organic Synthesis. *Curr. Org. Synth.* **2005**, *2*, 121–145. [CrossRef]
9. Bamberger, J.; Ostler, F.; Mancheno, O.G. Frontiers in Halogen and Chalcogen-Bond Donor Organocatalysis. *ChemCatChem* **2019**, *11*, 5198–5211. [CrossRef]
10. Vaish, A.; Tsarevsky, N.V. Hypervalent Iodine Compounds in Polymer Science and Technology. In *Main Group Strategies towards Functional Organic Materials*; Baumgartner, T., Jaekle, F., Eds.; Wiley: Chichester, UK, 2018; pp. 483–514. [CrossRef]
11. Musher, J.I. The Chemistry of Hypervalent Molecules. *Angew. Chem. Int. Ed.* **1969**, *8*, 54–68. [CrossRef]
12. Pimentel, G.C. The Bonding of Trihalide and Bifluoride Ions by the Molecular Orbital Method. *J. Chem. Phys.* **1951**, *19*, 446–448. [CrossRef]
13. Hach, R.J.; Rundle, R.E. The Structure of Tetramethylammonium Pentaiodide. *J. Am. Chem. Soc.* **1951**, *73*, 4321–4324. [CrossRef]
14. Munzarova, M.L.; Hoffmann, R. Electron-Rich Three-Center Bonding: Role of s,p Interactions across the p-Block. *J. Am. Chem. Soc.* **2002**, *124*, 4787–4795. [CrossRef]
15. Durrant, M.C. A quantitative definition of hypervalency. *Chem. Sci.* **2015**, *6*, 6614–6623. [CrossRef]
16. Kalemosa, A.; Ariyarathnab, I.R.; Khanb, S.N.; Miliordosb, E.; Mavridis, A. Hypervalency and the chemical bond. *Comput. Theoret. Chem.* **2019**, *1153*, 65–74. [CrossRef]
17. Crabtree, R.H. Hypervalency, secondary bonding and hydrogen bonding: Siblings under the skin. *Chem. Soc. Rev.* **2017**, *46*, 1720–1729. [CrossRef]
18. Kupwade, R.V. A Concise Review of Hypervalent Iodine with Special Reference to Dess- Martin Periodinane. *Mini-Rev. Org. Chem.* **2020**, *17*, 946-1–946-12. [CrossRef]
19. Yannacone, S.; Oliveira, V.; Verma, N.; Kraka, E. A Continuum from Halogen Bonds to Covalent Bonds: Where Do λ^3 Iodanes Fit? *Inorganics* **2019**, *7*, 47. [CrossRef]
20. Varvoglis, A. Aryliodine(III) Dicarboxylates. *Chem. Soc. Rev.* **1981**, *10*, 377. [CrossRef]
21. Waser, J. Benziodoxol(on)e Reagents as Tools in Organic Synthesis: The Background behind the Discovery at the Laboratory of Catalysis and Organic Synthesis. *Synlett* **2016**, *27*, 2761–2773. [CrossRef]
22. Ostrovskii, V.A.; Koldobskii, G.I.; Trifonov, R.E. Tetrazoles. In *Comprehensive Heterocyclic Chemistry III*; Katritzky, A.R., Ramsden, C.A., Scriven, E.F.V., Taylor, R.J.K., Eds.; Elsevier: Oxford, UK, 2008; pp. 257–423. [CrossRef]
23. Kumar, R.; Vaish, A.; Runčevski, T.; Tsarevsky, N.V. Hypervalent Iodine Compounds with Tetrazole Ligands. *J. Org. Chem.* **2018**, *83*, 12496–12506. [CrossRef] [PubMed]
24. Vaish, A.; Sayala, K.D.; Tsarevsky, N.V. N-Heterocycle (Tetrazole)-Stabilized Pseudocyclic λ^3-Iodane: Synthesis and Reactivity. *Tetrahedron Lett.* **2019**, *60*, 150995. [CrossRef]
25. Kumar, R.; Sayala, K.D.; Camdzic, L.L.; Siegler, M.; Vaish, A.; Tsarevsky, N. Heterocyclic Hypervalent Iodine(III) Compounds with Fused Benziodazole and Tetrazole Rings (I-Substituted Tetrazolo[1,5-b][1,2]Benziodazoles). *ChemRxiv* **2020**. [CrossRef]
26. Wang, T.; Gao, H.; Shreeve, J.M. Functionalized Tetrazole Energetics: A Route to Enhanced Performance. *Z. Anorg. Allg. Chem.* **2021**, *647*, 157–191. [CrossRef]

27. Singh, R.P.; Verma, R.D.; Meshri, D.T.; Shreeve, J.M. Energetic Nitrogen-Rich Salts and Ionic Liquids. *Angew. Chem. Int. Ed.* **2006**, *45*, 3584–3601. [CrossRef] [PubMed]
28. Trifonov, R.E.; Ostrovskii, V.A. Protolytic Equilibria in Tetrazoles. *Russ. J. Org. Chem.* **2006**, *42*, 1585–1605. [CrossRef]
29. Wani, M.Y.; Silva, M.R.; Krishnakumar, B.; Kumar, S.; Al-Bogami, A.S.; Aqlan, F.M.; Sobral, A.J.F.N. Catalytic Synthesis of 5-Substituted Tetrazoles: Unexpected Reactions and Products. *J. Heterocycl. Chem.* **2019**, *56*, 1613–1621. [CrossRef]
30. Koch, E.C. *High Explosives, Propellants, Pyrotechnics*; DeGruyter: Boston, MA, USA, 2021.
31. Dosch, D.E.; Reichel, M.; Born, M.; Klapötke, T.M.; Karaghiosoff, K. Investigation of Structure-Property Relationships of Three Nitroaromatic Compounds: 1-Fluoro-2,4,6-Trinitrobenzene, 2,4,6-Trinitrophenyl Methanesulfonate, and 2,4,6-Trinitrobenzaldehyde. *Cryst. Growth Des.* **2020**, *21*, 243–248. [CrossRef]
32. Li, J. Relationships for the Impact Sensitivities of Energetic C-Nitro Compounds Based on Bond Dissociation Energy. *J. Phys. Chem. B* **2010**, *114*, 2198–2202. [CrossRef] [PubMed]
33. Li, J. A Quantitative Relationship for the Shock Sensitivities of Energetic Compounds based on $X-NO_2$ (X = C, N, O) Bond Dissociation Energy. *J. Hazard. Mater.* **2010**, *180*, 768–772. [CrossRef] [PubMed]
34. Luo, Y.R. *Comprehensive Handbook of Chemical Bond Energies*; Taylor and Francis: Boca Raton, FL, USA, 2007.
35. Morse, M.D. Predissociation measurements of bond dissociation energies. *Acc. Chem. Res.* **2018**, *52*, 119–126. [CrossRef]
36. Zhang, J.; Zhang, Q.; Vo, T.T.; Parrish, D.A.; Shreeve, J.M. Energetic Salts with π-Stacking and Hydrogen-Bonding Interactions Lead the Way to Future Energetic Materials. *J. Am. Chem. Soc.* **2015**, *137*, 1697–1704. [CrossRef] [PubMed]
37. Cremer, D.; Kraka, E. From Molecular Vibrations to Bonding, Chemical Reactions, and Reaction Mechanism. *Curr. Org. Chem.* **2010**, *14*, 1524–1560. [CrossRef]
38. Kalescky, R.; Kraka, E.; Cremer, D. Are Carbon-Halogen Double and Triple Bonds Possible? *Int. J. Quantum Chem.* **2014**, *114*, 1060–1072. [CrossRef]
39. Kalescky, R.; Zou, W.; Kraka, E.; Cremer, D. Quantitative Assessment of the Multiplicity of Carbon-Halogen Bonds: Carbenium and Halonium Ions with F, Cl, Br, and I. *J. Phys. Chem. A* **2014**, *118*, 1948–1963. [CrossRef]
40. Oliveira, V.; Kraka, E.; Cremer, D. Quantitative Assessment of Halogen Bonding Utilizing Vibrational Spectroscopy. *Inorg. Chem.* **2016**, *56*, 488–502. [CrossRef] [PubMed]
41. Setiawan, D.; Sethio, D.; Cremer, D.; Kraka, E. From Strong to Weak NF Bonds: On the Design of a New Class of Fluorinating Agents. *Phys. Chem. Chem. Phys.* **2018**, *20*, 23913–23927. [CrossRef] [PubMed]
42. Sethio, D.; Oliveira, V.; Kraka, E. Quantitative Assessment of Tetrel Bonding Utilizing Vibrational Spectroscopy. *Molecules* **2018**, *23*, 2763. [CrossRef] [PubMed]
43. Grant, D.J.; Matus, M.H.; Switzer, J.R.; Dixon, D.A.; Francisco, J.S.; Christe, K.O. Bond Dissociation Energies in Second-Row Compounds. *J. Phys. Chem. A* **1966**, *112*, 3145–3156. [CrossRef] [PubMed]
44. Konkoli, Z.; Cremer, D. A New Way of Analyzing Vibrational Spectra. I. Derivation of Adiabatic Internal Modes. *Int. J. Quantum Chem.* **1998**, *67*, 1–9. [CrossRef]
45. Konkoli, Z.; Larsson, J.A.; Cremer, D. A New Way of Analyzing Vibrational Spectra. II. Comparison of Internal Mode Frequencies. *Int. J. Quantum Chem.* **1998**, *67*, 11–27. [CrossRef]
46. Konkoli, Z.; Cremer, D. A New Way of Analyzing Vibrational Spectra. III. Characterization of Normal Vibrational Modes in terms of Internal Vibrational Modes. *Int. J. Quantum Chem.* **1998**, *67*, 29–40. [CrossRef]
47. Konkoli, Z.; Larsson, J.A.; Cremer, D. A New Way of Analyzing Vibrational Spectra. IV. Application and Testing of Adiabatic Modes within the Concept of the Characterization of Normal Modes. *Int. J. Quantum Chem.* **1998**, *67*, 41–55. [CrossRef]
48. Cremer, D.; Larsson, J.A.; Kraka, E. New Developments in the Analysis of Vibrational Spectra on the Use of Adiabatic Internal Vibrational Modes. In *Theoretical and Computational Chemistry*; Parkanyi, C., Ed.; Elsevier: Amsterdam, The Netherlands, 1998; pp. 259–327.
49. Kraka, E.; Zou, W.; Tao, Y. Decoding Chemical Information from Vibrational Spectroscopy Data: Local Vibrational Mode Theory. *WIREs Comput. Mol. Sci.* **2020**, *10*, e1480. [CrossRef]
50. Klapötke, T.M. *Chemistry of High-Energy Materials*, 5th ed.; DeGruyter: Boston, MA, USA, 2019.
51. Kettner, M.A.; Klapötke, T.M. New Energetic Polynitrotetrazoles. *Chem. Eur. J.* **2015**, *21*, 3755–3765. [CrossRef]
52. Köhler, J.; Meyer, R.; Homburg, A. *Explosivstoffe*; Wiley: Weinheim, Germany, 2008.
53. Becke, A.D. Density-Functional Thermochemistry. III. The Role of Exact Exchange. *J. Chem. Phys.* **1993**, *98*, 5648–5652. [CrossRef]
54. Becke, A.D. A New Mixing of Hartree-Fock and Local Density-Functional Theories. *J. Chem. Phys.* **1993**, *98*, 1372–1377. [CrossRef]
55. Becke, A.D. Density-Functional Thermochemistry. V. Systematic Optimization of Exchange-Correlation Functionals. *J. Chem. Phys.* **1997**, *107*, 8554–8560. [CrossRef]
56. Salomon, O.; Reiher, M.; Hess, B.A. Assertion and Validation of the Performance of the B3LYP Functional for the First Transition Metal Row and the G2 Test Set. *J. Chem. Phys.* **2002**, *117*, 4729–4737. [CrossRef]
57. Grimme, S.; Antony, J.; Ehrlich, S.; Krieg, H. A Consistent and Accurate Ab Initio Parametrization of Density Functional Dispersion Correction (DFT-D) for the 94 Elements H-Pu. *J. Chem. Phys.* **2010**, *132*, 154104. [CrossRef] [PubMed]
58. Grimme, S.; Ehrlich, S.; Goerigk, L. Effect of the Damping Function in Dispersion Corrected Density Functional Theory. *J. Comput. Chem.* **2011**, *32*, 1456–1465. [CrossRef]

59. Zhao, Y.; Truhlar, D.G. The M06 Suite of Density Functionals for Main Group Thermochemstry, Thermochemical Kinetics, Noncovalent Interactions, Excited States, and Transition Elements: Two New Functionals and Systematic Testing of Four M06-Class Functionals and 12 Other Functionals. *Theor. Chem. Acc.* **2007**, *120*, 215–241.
60. Chai, J.D.; Head-Gordon, M. Long-Range Corrected Hybrid Density Functionals with Damped Atom-Atom Dispersion Corrections. *Phys. Chem. Chem. Phys.* **2008**, *10*, 6615–6620. [CrossRef]
61. Dunning, T.H. Gaussian Basis Sets for use in Correlated Molecular Calculations. I. The Atoms Boron through Neon and Hydrogen. *J. Chem. Phys.* **1989**, *90*, 1007–1023. [CrossRef]
62. Kendall, R.A.; Dunning, T.H.; Harrison, R.J. Electron Affinities of the First-Row Atoms Revisited. Systematic Basis Sets and Wave Functions. *J. Chem. Phys.* **1992**, *96*, 6796–6806. [CrossRef]
63. Woon, D.E.; Dunning, T.H. Gaussian Basis Sets for use in Correlated Molecular Calculations. III. The Atoms Aluminum through Argon. *J. Chem. Phys.* **1993**, *98*, 1358–1371. [CrossRef]
64. Woon, D.E.; Dunning, T.H. Gaussian Basis Sets for use in Correlated Molecular Calculations. IV. Calculation of Static Electrical Response Properties. *J. Chem. Phys.* **1994**, *100*, 2975–2988. [CrossRef]
65. Peterson, K.A. Systematically Convergent Basis Sets with Relativistic Pseudopotentials. I. Correlation Consistent Basis Sets for the Post-d Group 13-15 Elements. *J. Chem. Phys.* **2003**, *119*, 11099–11112. [CrossRef]
66. Peterson, K.A.; Figgen, D.; Goll, E.; Stoll, H.; Dolg, M. Systematically Convergent Basis Sets with Relativistic Pseudopotentials. II. Small-Core Pseudopotentials and Correlation Consistent Basis Sets for the Post-d Group 16-18 Elements. *J. Chem. Phys.* **2003**, *119*, 11113–11123. [CrossRef]
67. Schäfer, A.; Horn, H.; Ahlrichs, R. Fully optimized contracted Gaussian basis sets for atoms Li to Kr. *J. Chem. Phys.* **1992**, *97*, 2571–2577. [CrossRef]
68. Schäfer, A.; Huber, C.; Ahlrichs, R. Fully optimized contracted Gaussian basis sets of triple zeta valence quality for atoms Li to Kr. *J. Chem. Phys.* **1994**, *100*, 5829–5835. [CrossRef]
69. Weigend, F.; Ahlrichs, R. Balanced basis sets of split valence, triple zeta valence and quadruple zeta valence quality for H to Rn: Design and assessment of accuracy. *Phys. Chem. Chem. Phys.* **2005**, *7*, 3297. [CrossRef]
70. Weigend, F. Accurate Coulomb-fitting basis sets for H to Rn. *Phys. Chem. Chem. Phys.* **2006**, *8*, 1057–1065. [CrossRef]
71. Heinen, F.; Engelage, E.; Cramer, C.J.; Huber, S.M. Hypervalent Iodine(III) Compounds as Biaxial Halogen Bond Donors. *J. Am. Chem. Soc.* **2020**, *142*, 8633–8640. [CrossRef]
72. Sibert III, E.L. Modeling vibrational anharmonicity in infrared spectra of high frequency vibrations of polyatomic molecules. *J. Chem. Phys.* **2019**, *150*, 090901. [CrossRef]
73. Morse, M.D. Clusters of Transition-Metal Atoms. *Chem. Rev.* **1986**, *86*, 1049–1109. [CrossRef]
74. Byrd, E.F.C.; Sherrill, C.D.; Head-Gordon, M. The Theoretical Prediction of Molecular Radical Species: A Systematic Study of Equilibrium Geometries and Harmonic Vibrational Frequencies. *J. Phys. Chem. A* **2001**, *105*, 9736–9747. [CrossRef]
75. Coolidge, M.B.; Marlin, J.E.; Stewart, J.J.P. Calculations of Molecular Vibrational Frequencies using Semiempirical Methods. *J. Comput. Chem.* **1991**, *12*, 948–952. [CrossRef]
76. Galabov, B.; Yamaguchi, Y.; Remington, R.B.; Schaefer, H.F. High Level Ab Initio Quantum Mechanical Predictions of Infrared Intensities. *J. Phys. Chem. A* **2002**, *106*, 819–832. [CrossRef]
77. Halls, M.D.; Velkovski, J.; Schlegel, H.B. Harmonic Frequency Scaling Factors for Hartree-Fock, S-VWN, B-LYP, B3-LYP, B3-PW91 and MP2 with the Sadlej pVTZ Electric Property Basis Set. *Theor. Chem. Acc.* **2001**, *105*, 413–421. [CrossRef]
78. Irikura, K.K.; Johnson, R.D.; Kacker, R.N. Uncertainties in Scaling Factors for Ab Initio Vibrational Frequencies. *J. Phys. Chem. A* **2005**, *109*, 8430–8437. [CrossRef]
79. Scott, A.P.; Radom, L. Harmonic Vibrational Frequencies: An Evaluation of Hartree-Fock, Møller-Plesset, Quadratic Configuration Interaction, Density Functional Theory, and Semiempirical Scale Factors. *J. Phys. Chem.* **1996**, *100*, 16502–16513. [CrossRef]
80. Shefter, E.; Wolf, W. Crystal and Molecular Structure of 1,3Dihydro-1-hydroxy-3-oxo-1,2-benziodoxole. *Nature* **1964**, *203*, 512–513. [CrossRef]
81. Shefter, E.; Wolf, W. Crystal and Molecular Structure of 1,3Dihydro-1-hydroxy-3-oxo-1,2-benziodoxole. *J. Pharm. Sci.* **1965**, *54*, 104–107. [CrossRef]
82. Gräfenstein, J.; Cremer, D. Efficient DFT integrations by locally augmented radial grids. *J. Chem. Phys.* **2007**, *127*, 164113. [CrossRef]
83. Huang, Y.; Chang, C.; Yuan, J.; Zhao, Z. High-Harmonic and Terahertz Spectroscopy (HATS): Methods and Applications. *Appl. Sci.* **2019**, *9*, 853. [CrossRef]
84. Wu, G. *Vibrational Spectroscopy*; De Gruyter: Berlin, Germany, 2019.
85. Smith, E.; Dent, G. *Modern Raman Spectroscopy: A Practical Approach*; Wiley: New York, NY, USA, 2019.
86. Wilson, E.B.; Decius, J.C.; Cross, P.C. *Molecular Vibrations*; McGraw-Hill: New York, NY, USA, 1955.
87. Wilson, E.B., Jr. A Method of Obtaining the Expanded Secular Equation for the Vibration Frequencies of a Molecule. *J. Chem. Phys.* **1939**, *7*, 1047–1052. [CrossRef]
88. Woodward, L.A. *Introduction to the Theory of Molecular Vibrations and Vibrational Spectroscopy*; Oxford University Press: Oxford, UK, 1972.
89. Quack, M. Spectra and Dynamics of Coupled Vibrations in Polyatomic Molecules. *Annu. Rev. Phys. Chem.* **1990**, *41*, 839–874. [CrossRef]

90. Halonen, L. Local Mode Vibrations in Polyatomic Molecules. In *Advances in Chemical Physics*; Prigogine, I., Rice, S., Eds.; Wiley: New York, NY, USA, 1998; Volume 104, pp. 41–179.
91. Jensen, P. An introduction to the theory of local mode vibrations. *Mol. Phys.* **2000**, *98*, 1253–1285. [CrossRef]
92. Zou, W.; Cremer, D. C_2 in a Box: Determining its Intrinsic Bond Strength for the $X^1\ \Sigma^+_g$ Ground State. *Chem. Eur. J.* **2016**, *22*, 4087–4097. [CrossRef]
93. Oomens, J.; Kraka, E.; Nguyen, M.K.; Morton, T.M. Structure, Vibrational Spectra, and Unimolecular Dissociation of Gaseous 1-Fluoro-1-phenethyl Cations. *J. Phys. Chem. A* **2008**, *112*, 10774–10783. [CrossRef] [PubMed]
94. Zou, W.; Kalescky, R.; Kraka, E.; Cremer, D. Relating Normal Vibrational Modes to Local Vibrational Modes: Benzene and Naphthalene. *J. Mol. Model.* **2012**, *19*, 2865–2877. [CrossRef] [PubMed]
95. Kalescky, R.; Kraka, E.; Cremer, D. Identification of the Strongest Bonds in Chemistry. *J. Phys. Chem. A* **2013**, *117*, 8981–8995. [CrossRef]
96. Kalescky, R.; Kraka, E.; Cremer, D. Description of Aromaticity with the Help of Vibrational Spectroscopy: Anthracene and Phenanthrene. *J. Phys. Chem. A* **2013**, *118*, 223–237. [CrossRef] [PubMed]
97. Kalescky, R.; Kraka, E.; Cremer, D. New Approach to Tolman's Electronic Parameter Based on Local Vibrational Modes. *Inorg. Chem.* **2013**, *53*, 478–495. [CrossRef]
98. Humason, A.; Zou, W.; Cremer, D. 11,11Dimethyl-1,6-methano[10]annulene-An Annulene with an Ultralong CC Bond or a Fluxional Molecule? *J. Phys. Chem A.* **2014**, *119*, 1666–1682. [CrossRef] [PubMed]
99. Sethio, D.; Lawson Daku, L.M.; Hagemann, H.; Kraka, E. Quantitative Assessment of B−B−B, B−H_b−B, and B−H_t Bonds: From BH_3 to $B_{12}H_{12}{}^{2-}$. *ChemPhysChem* **2019**, *20*, 1967–1977. [CrossRef]
100. Makoś, M.Z.; Freindorf, M.; Sethio, D.; Kraka, E. New Insights into Fe-H_2 and Fe-H^- Bonding of a [NiFe] Hydrogenase Mimic–A Local Vibrational Mode Study. *Theor. Chem. Acc.* **2019**, *138*, 76. [CrossRef]
101. Makoś, M.Z.; Zou, W.; Freindorf, M.; Kraka, E. Metal-Ring Interactions in Actinide Sandwich Compounds: A Combined Normalized Elimination of the Small Component and Local Vibrational Mode Study. *Mol. Phys.* **2020**, *118*, e1768314. [CrossRef]
102. Verma, N.; Tao, Y.; Zou, W.; Chen, X.; Chen, X.; Freindorf, M.; Kraka, E. A Critical Evaluation of Vibrational Stark Effect (VSE) Probes with the Local Vibrational Mode Theory. *Sensors* **2020**, *20*, 2358. [CrossRef]
103. Freindorf, M.; Kraka, E. Critical Assessment of the FeC and CO Bond strength in Carboxymyoglobin–A QM/MM Local Vibrational Mode Study. *J. Mol. Model.* **2020**, *26*, 281-1–281-15. [CrossRef] [PubMed]
104. Kraka, E.; Freindorf, M. Characterizing the Metal Ligand Bond Strength via Vibrational Spectroscopy: The Metal Ligand Electronic Parameter (MLEP). In *Topics in Organometallic Chemistry–New Directions in the Modeling of Organometallic Reactions*; Lledós, A., Ujaque, G., Eds.; Springer: Berlin/Heidelberg, Germany, 2020; Volume 67, pp. 1–43.
105. Freindorf, M.; Kraka, E.; Cremer, D. A Comprehensive Analysis of Hydrogen Bond Interactions Based on Local Vibrational Modes. *Int. J. Quantum Chem.* **2012**, *112*, 3174–3187. [CrossRef]
106. Kalescky, R.; Zou, W.; Kraka, E.; Cremer, D. Local Vibrational Modes of the Water Dimer–Comparison of Theory and Experiment. *Chem. Phys. Lett.* **2012**, *554*, 243–247. [CrossRef]
107. Kalescky, R.; Kraka, E.; Cremer, D. Local Vibrational Modes of the Formic Acid Dimer–The Strength of the Double H-Bond. *Mol. Phys.* **2013**, *111*, 1497–1510. [CrossRef]
108. Kraka, E.; Freindorf, M.; Cremer, D. Chiral Discrimination by Vibrational Spectroscopy Utilizing Local Modes. *Chirality* **2013**, *25*, 185–196. [CrossRef]
109. Setiawan, D.; Kraka, E.; Cremer, D. Description of Pnicogen Bonding with the help of Vibrational Spectroscopy-The Missing Link between Theory and Experiment. *Chem. Phys. Lett.* **2014**, *614*, 136–142. [CrossRef]
110. Setiawan, D.; Kraka, E.; Cremer, D. Strength of the Pnicogen Bond in Complexes Involving Group VA Elements N, P, and As. *J. Phys. Chem. A* **2014**, *119*, 1642–1656. [CrossRef]
111. Setiawan, D.; Kraka, E.; Cremer, D. Hidden Bond Anomalies: The Peculiar Case of the Fluorinated Amine Chalcogenides. *J. Phys. Chem. A* **2015**, *119*, 9541–9556. [CrossRef] [PubMed]
112. Kraka, E.; Setiawan, D.; Cremer, D. Re-Evaluation of the Bond Length-Bond Strength Rule: The Stronger Bond Is not Always the Shorter Bond. *J. Comp. Chem.* **2015**, *37*, 130–142. [CrossRef] [PubMed]
113. Zhang, X.; Dai, H.; Yan, H.; Zou, W.; Cremer, D. B-H π Interaction: A New Type of Nonclassical Hydrogen Bonding. *J. Am. Chem. Soc.* **2016**, *138*, 4334–4337. [CrossRef]
114. Setiawan, D.; Cremer, D. Super-Pnicogen Bonding in the Radical Anion of the Fluorophosphine Dimer. *Chem. Phys. Lett.* **2016**, *662*, 182–187. [CrossRef]
115. Oliveira, V.; Kraka, E.; Cremer, D. The Intrinsic Strength of the Halogen Bond: Electrostatic and Covalent Contributions Described by Coupled Cluster Theory. *Phys. Chem. Chem. Phys.* **2016**, *18*, 33031–33046. [CrossRef]
116. Tao, Y.; Zou, W.; Jia, J.; Li, W.; Cremer, D. Different Ways of Hydrogen Bonding in Water–Why Does Warm Water Freeze Faster than Cold Water? *J. Chem. Theory Comput.* **2017**, *13*, 55–76. [CrossRef]
117. Oliveira, V.; Cremer, D. Transition from Metal-Ligand Bonding to Halogen Bonding Involving a Metal as Halogen Acceptor: A Study of Cu, Ag, Au, Pt, and Hg Complexes. *Chem. Phys. Lett.* **2017**, *681*, 56–63. [CrossRef]
118. Oliveira, V.; Cremer, D.; Kraka, E. The Many Facets of Chalcogen Bonding: Described by Vibrational Spectroscopy. *J. Phys. Chem. A* **2017**, *121*, 6845–6862. [CrossRef] [PubMed]

119. Oliveira, V.; Kraka, E. Systematic Coupled Cluster Study of Noncovalent Interactions Involving Halogens, Chalcogens, and Pnicogens. *J. Phys. Chem. A* **2017**, *121*, 9544–9556. [CrossRef] [PubMed]
120. Zou, W.; Zhang, X.; Dai, H.; Yan, H.; Cremer, D.; Kraka, E. Description of an Unusual Hydrogen Bond Between Carborane and a Phenyl Group. *J. Organometal. Chem.* **2018**, *856*, 114–127. [CrossRef]
121. Lyu, S.; Beiranvand, N.; Freindorf, M.; Kraka, E. Interplay of Ring Puckering and Hydrogen Bonding in Deoxyribonucleosides. *J. Phys. Chem. A* **2019**, *123*, 7087–7103. [CrossRef]
122. Oliveira, V.P.; Marcial, B.L.; Machado, F.B.C.; Kraka, E. Metal-Halogen Bonding Seen through the Eyes of Vibrational Spectroscopy. *Materials* **2020**, *13*, 55. [CrossRef] [PubMed]
123. Tao, Y.; Qiu, Y.; Zou, W.; Nanayakkara, S.; Yannacone, S.; Kraka, E. In Situ Assessment of Intrinsic Strength of X-I$\cdots$OA Type Halogen Bonds in Molecular Crystals with Periodic Local Vibrational Mode Theory. *Molecules* **2020**, *25*, 1589. [CrossRef]
124. Yannacone, S.; Sethio, D.; Kraka, E. Quantitative Assessment of Intramolecular Hydrogen Bonds in Neutral Histidine. *Theor. Chem. Acc.* **2020**, *139*, 125-1–125-10. [CrossRef]
125. Martins, J.; Quintino, R.P.; Politi, J.R.S.; Sethio, D.; Gargano, R.; Kraka, E. Computational Analysis of Vibrational Frequencies and Rovibrational Spectroscopic Constants of Hydrogen Sulfide Dimer using MP2 and CCSD(T). *Spectrochim. Acta A* **2020**, *239*, 118540-1–118540-9. [CrossRef]
126. Yannacone, S.; Freindorf, M.; Tao, Y.; Zou, W.; Kraka, E. Local Vibrational Mode Analysis of π-Hole Interactions between Aryl Donors and Small Molecule Acceptors. *Crystals* **2020**, *10*, 556. [CrossRef]
127. Frisch, M.J.; Trucks, G.W.; Schlegel, H.B.; Scuseria, G.E.; Robb, M.A.; Cheeseman, J.R.; Scalmani, G.; Barone, V.; Petersson, G.A.; Nakatsuji, H.; et al. *Gaussian16 Revision B.01*; Gaussian Inc.: Wallingford, CT, USA, 2016.
128. Zou, W.; Tao, Y.; Freindorf, M.; Makoś, M.Z.; Verma, N.; Kraka, E. *Local Vibrational Mode Analysis (LModeA)*; Computational and Theoretical Chemistry Group (CATCO), Southern Methodist University: Dallas, TX, USA, 2020.
129. Reed, A.E.; Curtiss, L.A.; Weinhold, F. Intermolecular Interactions from a Natural Bond Orbital, Donor-Acceptor Viewpoint. *Chem. Rev.* **1988**, *88*, 899–926. [CrossRef]
130. Weinhold, F.; Landis, C.R. *Valency and Bonding: A Natural Bond Orbital Donor-Acceptor Perspective*; Cambridge University Press: Cambridge, UK, 2005.
131. Weinhold, F.; Landis, C.R.; Glendening, E.D. What is NBO Analysis and How is it Useful? *Int. Rev. Phys. Chem.* **2016**, *35*, 39–440. [CrossRef]
132. Keith, T.A. AIMAll (Version 17.11.14). 2017. Available online: aim.tkgristmill.com (accessed on 12 May 2021).
133. Cremer, D.; Kraka, E. Chemical Bonds without Bonding Electron Density? Does the Difference Electron-Density Analysis Suffice for a Description of the Chemical Bond? *Angew. Chem. Int. Ed.* **1984**, *23*, 627–628. [CrossRef]
134. Cremer, D.; Kraka, E. A Description of the Chemical Bond in Terms of Local Properties of Electron Density and Energy. *Croat. Chem. Acta* **1984**, *57*, 1259–1281.
135. Kraka, E.; Cremer, D. Chemical Implication of Local Features of the Electron Density Distribution. In *Theoretical Models of Chemical Bonding. The Concept of the Chemical Bond*; Maksic, Z.B., Ed.; Springer: Berlin/Heidelberg, Germany, 1990; Volume 2, pp. 453–542.
136. Kraszkiewicz, L.; Skulski, L. Optimized syntheses of iodylarenes from iodoarenes, with sodium periodate as the oxidant. Part II. *Arkivoc* **2003**, *2003*, 120–125. [CrossRef]
137. *Origin(Pro) 9.1.0 (64 bit)*; OriginLab Corporation: Northampton, MA, USA, 2013.
138. Kaczmarek, J.; Grzonka, Z. Substituent Effects in Infrared Absorption Spectra of 5-Phenyltetrazoles. *Pol. J. Chem.* **1980**, *54*, 1297–1300.
139. Matveeva, N.A.; Sushko, N.I.; Makarevich, N.I.; Gaponik, P.N.; Ivashkevich, O.A.; Koren, A.O. Substituent Effects in Infrared Absorption Spectra of 5-Phenyltetrazoles. *Zh. Prikl. Spektrosk.* **1992**, *57*, 442–450.
140. Rogachev, A.Y.; Hoffmann, R. Iodine (I_2) as a Janus-Faced Ligand in Organometallics. *J. Am. Chem. Soc.* **2013**, *135*, 3262–3275. [CrossRef] [PubMed]
141. Boyer, J.H.; Miller, E.J. The Tetrazole-Azidoazomethine Equilibrium. *J. Am. Chem. Soc.* **1959**, *81*, 4671–4673. [CrossRef]
142. Henry, R.A.; Finnegan, W.G.; Lieber, E. Kinetics of the Isomerization of Substituted 5-Aminotetrazoles. *J. Am. Chem. Soc.* **1955**, *77*, 2264–2270. [CrossRef]
143. Lieber, E.; Rao, C.N.R.; Chao, T.S.; Ramachandran, J. Relative Acidities of 5-(Substituted Phenyl)amino-4-phenyl-1,2,3-triazoles. *J. Org. Chem.* **1958**, *23*, 1916–1918. [CrossRef]
144. Sanderson, R. *Polar Covalence*; Academic Press: New York, NY, USA, 1983.
145. Courtois, B. Découverte d'une substance nouvelle dans le varech. *Ann. Chim.* **1813**, *88*, 304–310.
146. Silberrad, O. IX.–The Constitution of Nitrogen Iodide. *J. Chem. Soc. Trans.* **1905**, *87*, 55–66. [CrossRef]